REPORT DOCUMENTATION PAGE

Form Approved OMB No. 0704-0188

Public reporting burden for this collection of information is estimated to average 1 hour per response, including the time for reviewing instructions, searching existing data sources, gathering and maintaining the data needed, and completing and reviewing the collection of information. Send comments regarding this burden estimate or any other aspect of this collection of information, including suggestions for reducing the burden, to Department of Defense, Washington Headquarters Services, Directorate for Information Operations and Reports (0704-0188), 1215 Jefferson Davis Highway, Suite 1204, Arlington, VA 22202-4302. Respondents should be aware that notwithstanding any other provision of law, no person shall be subject to any penalty for failing to comply with a collection of information if it does not display a currently valid OMB control number.
PLEASE DO NOT RETURN YOUR FORM TO THE ABOVE ADDRESS.

1. REPORT DATE *(DD-MM-YYYY)*
12-06-2009

2. REPORT TYPE
Final Report

3. DATES COVERED *(From – To)*
1 January 2007 - 13-Jun-10

4. TITLE AND SUBTITLE
Hypersonic Induced Interactions of Plasma and Non-Plasma Jets

5a. CONTRACT NUMBER
FA8655-07-1-3032

5b. GRANT NUMBER

5c. PROGRAM ELEMENT NUMBER

6. AUTHOR(S)
Professor Konstantinos Kontis

5d. PROJECT NUMBER

5d. TASK NUMBER

5e. WORK UNIT NUMBER

7. PERFORMING ORGANIZATION NAME(S) AND ADDRESS(ES)
University of Manchester
GB/44, Sackville Street
Manchester M60 1QD
United Kingdom

8. PERFORMING ORGANIZATION REPORT NUMBER
N/A

9. SPONSORING/MONITORING AGENCY NAME(S) AND ADDRESS(ES)
EOARD
Unit 4515 BOX 14
APO AE 09421

10. SPONSOR/MONITOR'S ACRONYM(S)

11. SPONSOR/MONITOR'S REPORT NUMBER(S)
Grant 07-3032

12. DISTRIBUTION/AVAILABILITY STATEMENT
Approved for public release; distribution is unlimited.

13. SUPPLEMENTARY NOTES

14. ABSTRACT

This report results from a contract tasking University of Manchester as follows: The investigation will be conducted in the University of Manchester hypersonic blowdown wind tunnel facility (HSST) at Mach no. 4 to 6. All experimental tasks will utilize the following experimental techniques: i) Particle Image Velocimetry (PIV) and laser sheet; ii) Intensity-based in-house developed Pressure Sensitive Paint (PSP) imaging system; iii) Pressure tapings; iv) Pitot pressure and total temperature probes; v) Oil flow; and vi) High-speed phase-locked schlieren photography and double exposure holographic interferometry.
Task 1: Plasma and non-plasma (PnP) jet system and model design, and performance tests.
Task 2: Transverse non-plasma jet interaction tests: Investigation of the physics of transverse non-plasma jet interactions and determination of penetration distance of the jet into the cross-flow and separation lateral spreading.
Task 3: Active control of transverse jet interaction using localized arc filament plasma actuators (LAFPA): 3.1 Investigation of the physics of transverse jet interactions with LAFPA and determination of penetration distance of the jet into the cross-flow and separation lateral spreading; 3.2 Evaluation of the benefits of LAFPA system to enhance mixing of the jet with the cross flow fluid through modification of instabilities.
Task 4: Transverse plasma jet interaction tests: Investigation of the physics of transverse plasma jet interactions and determination of penetration distance of the jet into the cross-flow and separation lateral spreading.
Milestones:
Year 1: Transverse non-plasma jet interaction studies and baseline studies on localized arc filament plasma actuator (LAFPA) system design.
Year 2: Active control of transverse jet interaction using localized arc filament plasma actuators (LAFPA).
Year 3: Transverse plasma jet interaction studies.
Deliverables:
a. Interim quarterly reports and comprehensive final report at the end of each year;
b. Database on transverse plasma and non-plasma jet interactions;
c. Tools: methods and scaling laws for jet interaction technology;
d. Standards: evaluation of the benefits of LAFPA system to enhance mixing of the jet with the cross flow fluid through modification of instabilities.

15. SUBJECT TERMS
EOARD, Aerodyanamics, Hypersonic Flow

16. SECURITY CLASSIFICATION OF:			17. LIMITATION OF ABSTRACT	18, NUMBER OF PAGES	19a. NAME OF RESPONSIBLE PERSON
a. REPORT	b. ABSTRACT	c. THIS PAGE			SURYA SURAMPUDI
UNCLAS	UNCLAS	UNCLAS	UL	32	19b. TELEPHONE NUMBER *(Include area code)* +44 (0)1895 616021

Standard Form 298 (Rev. 8/98)
Prescribed by ANSI Std. Z39-18

FINAL REPORT: FA8655-07-1-3032

HYPERSONIC INDUCED INTERACTIONS OF PLASMA / NON-PLASMA JETS

Senior Assoc. Prof. Dr. Eur.Ing. K. Kontis
Aero-Physics Laboratory
School of MACE, GB-C43, Sackville Street
University of Manchester, Manchester, UK

ABSTRACT

Calibration of the tunnel, experimental setup of the clean case study and review of the state of the art were conducted. The prominent flow structures occurring on the turbulent boundary layer of a flat plate were investigated and their dependence on upstream conditions such as free-stream Reynolds no. was determined. Baseline transverse non-plasma jet interaction studies were performed. The investigation was conducted in the University of Manchester hypersonic blowdown wind tunnel at Mach no. 5 and free-stream Reynolds no. 6.5×10^6 to 13.5×10^6 per metre. The experimental tasks utilized high speed PIV, pressure tapings, and schlieren photography. The results were compared with numerical simulations performed using a 3-D time-marching Navier-Stokes code. Theoretical algorithms have been developed to predict the shape of the separation front and jet penetration height. The parameters, which determine the upstream extend and lateral spreading of the separation front around the transverse jet, and the magnitude of the separated region, are detailed. The design and manufacture of the plasma generation system was conducted. The instrumented jet nozzles were designed and manufactured. The PSP system was validated for high speed jet flow studies. The S/N, seeding quality and uniformity of the PIV system were optimised. A preliminary assessment of the effects of plasma actuators on jet and jet in crossflow was conducted.

NOMENCLATURE

C	Chapman-Rubesin constant
C_d	nose drag coefficient
d	diameter
h	height
L	length
M	Mach number
P	pressure
R	radius
Re	Reynolds number
T	temperature
x	measured distance in x-direction
y	measured distance in y-direction
Greek letters	
α	incidence
β	flare angle
γ	ratio of specific heats
ε	$(\gamma-1)/(\gamma+1)$
κ_ε	bluntness parameter, $M^3C_d\varepsilon(d_n/x)$
χ	viscous interaction parameter for laminar flow, $M_\infty^3\sqrt{C/\mathrm{Re}_x}$
χ_ε	$\varepsilon[0.664+1.73(T_w/T_o)]\chi$
ψ	jet bow shock stand-off distance
subscripts	
∞	Free stream
2	local undisturbed value

fp	flat-plate
j	jet
n	nose of flat plate
o	total
sep	separation
w	wall

1. INTRODUCTION

Shockwave/boundary layer interactions, one of the most commonly encountered complex flow structures on the surfaces of supersonic/ hypersonic vehicles, have been an active research topic for many years. The reason for attention is the fact that shockwaves impose severely turbulent and unsteady separations on boundary layers on the flight surfaces which can cause mechanical fatigue of aero-structures and excessive heat transfer rates [1]. The unsteadiness observed in the interactions spans a wide range of frequencies and scales. Many authors have characterized the interaction unsteadiness as the motion of the separation shock foot [1,2]. It has been observed that the dominant frequency range that characterizes the shock-foot motion is at least an order of magnitude lower than the nominal boundary layer frequency based on freestream velocity and boundary layer thickness $(U_\infty/\delta)^2$. The explanation of this low-frequency motion of the shock foot has been ambiguous due to the difficulty in relating low frequencies with typical turbulent mechanisms; the low frequency motion of the shock foot seems to be related to the low-frequency motion of the separated flow [3]. Furthermore, various studies of different interactive flows have investigated the unsteady nature of the separation shock foot and in turn the unsteadiness of the separation bubble and have concluded that there is a relationship between the observed unsteady motion and the upstream turbulent boundary layer, which is associated with upstream Reynolds number. There is emerging evidence that the low-frequency unsteadiness is driven by low frequency turbulent fluctuations in the upstream turbulent boundary layer [4-5].

Hypersonic flight within the atmosphere is of current interest, both military and civilian. Secondary fluid injection is proposed as an attractive method of controlling the flight path, in situations where conventional aerodynamic surfaces cannot function properly, due either to the low density of the medium or to the considerable aerodynamic heating effects, [6-13]. Injection of plasma and non-plasma supersonic jets towards on-coming flow can be used to decelerate a flight vehicle and to reduce its drag and heat transfer, [14-17]. Jet interactions are applicable in the investigation of the mixing characteristics of fuel injection with incoming flows in scramjet configurations, [18]. Even under ideal conditions, scramjets powered hypersonic vehicles have very small thrust margins, [19]. Thus, a key goal in scramjet design is efficient fuel-air combustion. The challenges associated with this goal are (1) the injection into the supersonic flow produces shock waves, which create drag, (2) the resident time of the fuel within the combustor is on the order of 1-2 milliseconds, (3) compressibility hinders mixing, and (4) low loss flame holding. Turbulence plays an important role in enhancing fuel-air mixing. Hence, characterization of the behavior of turbulence in jet interaction flow fields, encountered in fuel injection applications in air-breathing propulsion systems, is beneficial to understanding and improve the mixing process, [20].

The interaction of a transverse control jet with the local cross flow creates a highly three-dimensional adverse pressure gradient. This generates a three-dimensional highly unsteady separated interaction region containing subsonic and supersonic regions, rotational flows, mixing layers, thermal gradients etc. The complexity of flow fields created by jets interacting with external flows is such that the present understanding of them relies heavily on experimental data, [21]. These features make the flow field very complicated, difficult to describe, and model. However, these strong secondary motions also provide an opportunity for flow control to tailor the flow, [22-23]. For example, Srinivasan and Bowersox [24] developed a method using a diamond shaped orifice to introduce a gas-dynamically induced trapped vortex pair. This vortex pair has the potential to serve as flame holder. Further, Srinivasan and Bowersox were also able to tailor the flow to enhance the mixing through enhance vorticity production near the

leading edge of the injector. Data about the unsteady characteristics of such type of flows is practically absent, especially on the induced pressure fluctuations on the part of the surface located in the region of separated flow in front of and behind the jet. The pressure fluctuation field is a source of vibrations and it has to be taken into consideration when analysing the structure dynamic characteristics, fatigue strength and acoustic effect on devices and equipment. There is a qualitative analogy between the interaction of the flow with solid and gaseous obstacles. Nevertheless, the specific character of jet formation and interaction does not allow using directly the trends and normalized data deduced by investigations using solid obstacles.

The introduction of bluntness modifies the aerodynamic properties of the flow over a flat-plate body from that with an equivalent sharp leading edge. The bow shock wave stands off from the leading edge and is highly curved, which give rise to gradients in flow properties normal to the plate surface. The stream tubes crossing the shock near the leading edge suffer a large entropy rise and then expand rapidly downstream. This entropy layer is a region of high temperature and low density, with total pressure losses due to the bow shock and lower local Mach number and unit Reynolds number than in the free stream. The entropy layer influences the local flow conditions for a large distance downstream, and eventually it is swallowed by the boundary layer. Simpkins [25] found that the introduction of nose bluntness promotes separation. He did an experimental comparison of the interaction between a radial under expanded jet and the hypersonic flow over a sharp and a blunt cone of semi-angle 5 deg at a free stream Mach number of 13, with laminar boundary layers. Whereas, Kontis et al [26] found that nose bluntness causes a delay in separation with respect to the equivalent sharp cone configuration on experiments over a sharp and a blunt cone of 5 deg semi-angle at a free stream Mach number of 8.2, with laminar boundary layers. Kumar [27] identified some of the parameters that determine the upstream extent and lateral spreading of the separation front around an under expanded transverse jet on a slender blunted cone, under laminar conditions.

a.“small” bluntness condition:

Pressure distribution measurements conducted by Vermeulen et al [28] at M_∞=6 on a flat-plates with a slightly blunt leading edge showed the promotion of separation due to bluntness. Promotion of separation by leading edge bluntness was also observed by Edwards et al [29] in low density tests at M_∞=12.5 and $Re_\infty/m=6.2\times10^4$. In summary, for entirely laminar flow small bluntness promotes separation.

b.“large” bluntness condition:

In tests at M_∞=10.0 and $Re_\infty/m=8.4\times10^6$ on flat-plates, Coet et al [30] observed a delay in separation due to the introduction of d_n=0.0025 m and d_n=0.005 m hemi-cylindrical leading edge bluntness. Along with a reduction in the extent of the separation region, these tests showed an order of magnitude decrease in the separated region heat transfer due to leading edge bluntness. Pressure measurements conducted by Townsend [31] on a blunted flat plate configuration at M_∞=10.0 and $Re_\infty/m=5.0\times10^6$ showed an appreciable reduction in the extent of the separated flow region when leading edge bluntness was introduced. The state of the boundary layer was diagnosed as being laminar.

Measurements on flat plates by Holden et al [32] at M_∞=19 and β=25.7° showed that the extent of the laminar separated region was related to the viscous bluntness interaction parameter, $\chi_\varepsilon / \kappa_\varepsilon^{\frac{2}{3}} \sim M / \left[d_n^{2/3} \sqrt{Re_x} \right]$. This effectively accounted for the relative effects of changes in Mach number and Reynolds number on the extent of the interaction. Holden's results indicate that for $\chi_\varepsilon / \kappa_\varepsilon^{\frac{2}{3}} \le 0.1$, the introduction of leading edge bluntness results in a reduction in the extent of boundary layer separation. This is similar to the “large” bluntness condition discussed above. For $0.1 \le \chi_\varepsilon / \kappa_\varepsilon^{\frac{2}{3}} \le 0.5$, Holden observed that leading edge bluntness promotes separation. This is typical of the “small” bluntness condition discussed above. Due to the relatively high Mach number and the low free stream unit Reynolds number, it is believed that these tests were entirely laminar. In summary, bluntness has a dual effect on laminar separation: “Small” bluntness promotes separation of a laminar boundary layer (with respect to equivalent sharp configuration) while “large” bluntness delays separation.

The overall aim of the research is to improve our understanding on the physics and performance benefits of transverse plasma and non-plasma jet-induced interactions in high speed flows and to examine the benefits of localized arc filament plasma actuators to enhance mixing of the jet fluid with the cross flow fluid through modification of instabilities. The year 1 research activities included the following tasks: a) Investigation of the prominent flow structures occurring on the turbulent boundary layer of a flat plate and determination of their dependence on upstream conditions such as free-stream Reynolds no. (clean-case); and b) Baseline transverse non-plasma jet interaction studies. The year 2 research activities included the following tasks: a) Design and manufacture of the plasma actuator jet system; b) Validation of the PSP system for high speed jet studies; c) Baseline studies on localized arc filament plasma actuator system design; and d) Model integration and preliminary assessment of plasma actuators control effectiveness. The associated milestones are shown below:

Milestone	Task	Time [months]
M1	Calibration of the tunnel, experimental setup of the clean case study and review of the state of the art	5
M2	Clean case tests	8
M3	Non-plasma jet interaction model and system design, model integration and performance tests, and review of the state of the art	10
M4	Transverse non-plasma jet interaction tests: Phase A	12
M5	Design and manufacture of the plasma generation system	16
M6	Design and manufacture of the instrumented jet nozzles	17
M7	Validation of the PSP system for high speed jet studies	18
M8	Transverse non-plasma jet interaction tests: Phase B	20
M9	Baseline studies on localized arc filament plasma actuator system design	22
M10	Localized arc filament plasma actuator (LAFPA) system design, model integration and preliminary performance tests	24

2. EXPERIMENTAL SETUP

The investigation was conducted in the University of Manchester hypersonic blowdown wind tunnel facility (HSST) at Mach no. 5 and free-stream Reynolds no. 6.5×10^6 to 13.5×10^6 per metre. A schematic diagram of the tunnel is shown in Figure 1.

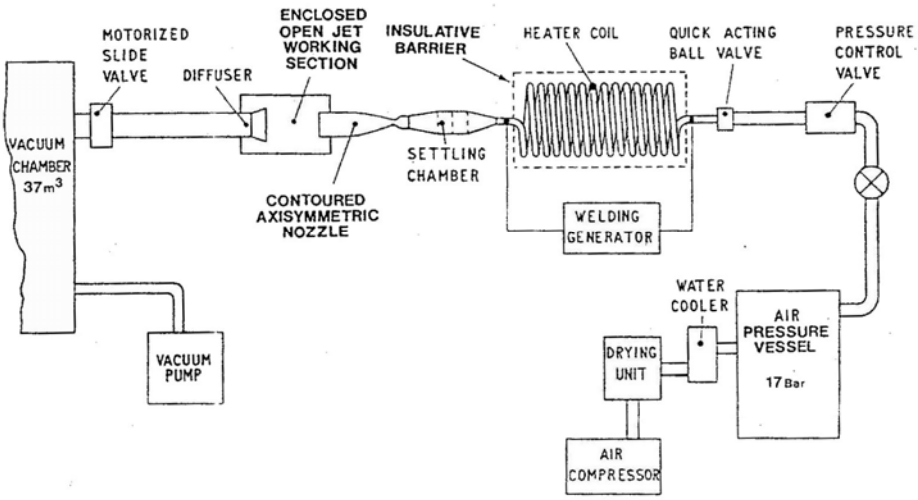

Figure 1: Schematic diagram of the HSST.

In this facility air is passed through a drying unit and stored in a high-pressure vessel. Control of the tunnel operating pressure is achieved through a dome valve situated at the exit of the

pressure vessel. This enables the tunnel pressure to be set up to 13.8 x 10^5 N/m^2 (200 psi). To avoid liquefaction, the air is passed through a 30m long heater coil which can be set up to 800 K. This heater coil is embedded in an insulated box. After passing through the heater coil the air enters the settling chamber, designed to give a uniform flow distribution in the working section. The working section accommodates two vertical schlieren windows to allow flow visualisation and four access ports. The diffuser is placed 0.4m downstream from the nozzle exit. A motorised slide valve is positioned between the working section and the vacuum tank. This allows access to the working section without pressurising the vacuum tank, between runs. Variation of the Reynolds number is possible by the setting of different supply pressures and heater temperatures. For a typical supply pressure setting of 190 psi, the Reynolds number ranges from 5.5x10^6 to 11.5x10^6 for heater temperature settings between 370° K and 550° K, see Fig. 2. The total temperature measured within the freestream increases linearly with heater temperature settings, Fig. 3. In all cases the heater temperature is higher than the recorded total temperature. The flow is started through the opening of a fast acting ball valve, situated between the dome valve and heater coil. Useful flow run times this wind tunnel range from 7 to 10 seconds depending upon the supply pressure setting. Three axisymmetric nozzles for flow at Mach 4, 5 and 6 are available for use in this tunnel. A further Mach 5 nozzle, incorporating 50mm or 30 mm diameter centre body, is also available.

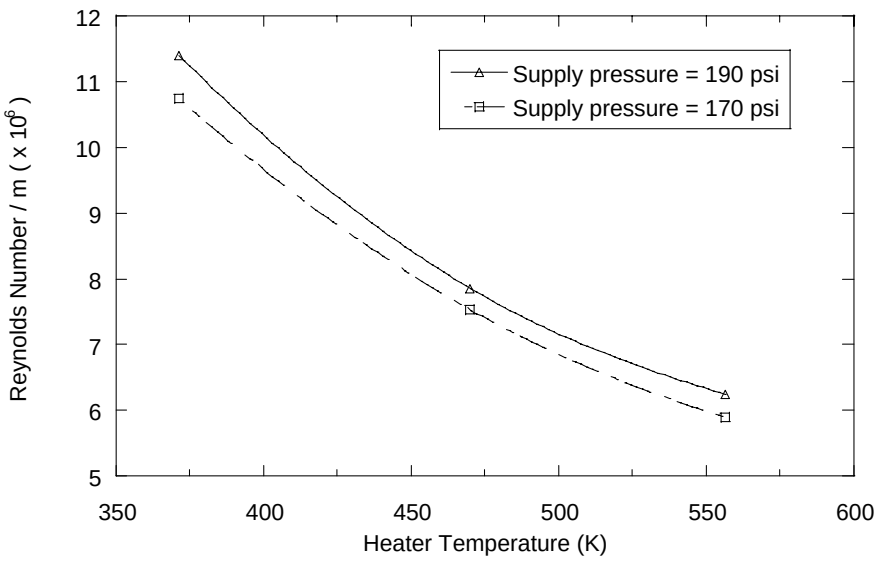

Figure 2: Variation of Reynolds number through supply pressure and heater settings

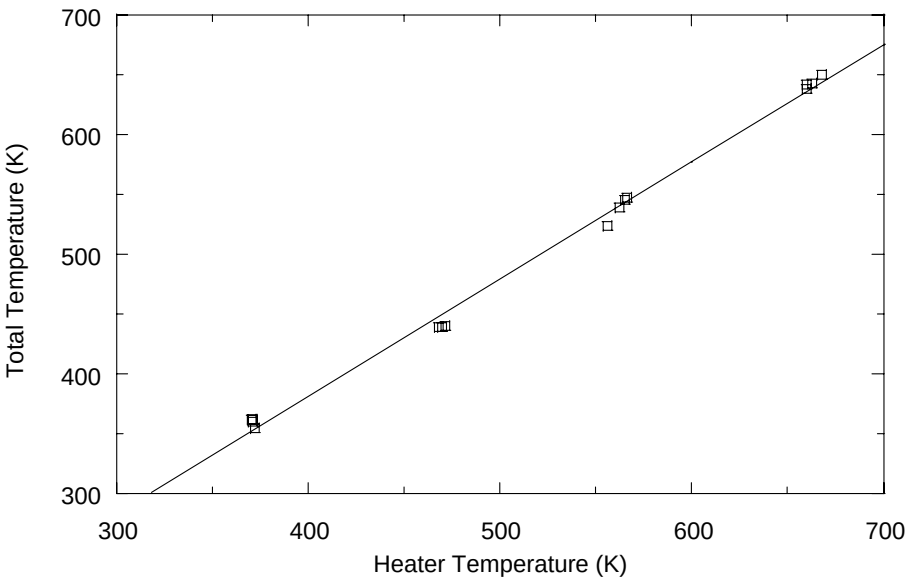

Figure 3: Variation of total temperature with heater temperature

Figure 4 shows the recorded pressures in the settling chamber for three runs using an operating pressure setting of 1.3 x 106 N/m^2 (190psi) and heater settings of 373K, 474K and 573K. As the flow in the settling chamber is subsonic, the recorded pressures are the reservoir pressures. This figure shows that pressure increases to steady operating conditions within 1 second of start up. For the three runs shown, the level of reservoir pressure is seen to vary by 6.5%. Further variations in reservoir pressure are seen to occur during the runs. This variation appears to be influenced by the heater temperature. At heater settings of 573K the reservoir pressure increases by 1.7% during the run while reductions of 1.2% and 1% are observed for 373K and 473 K heater settings respectively.

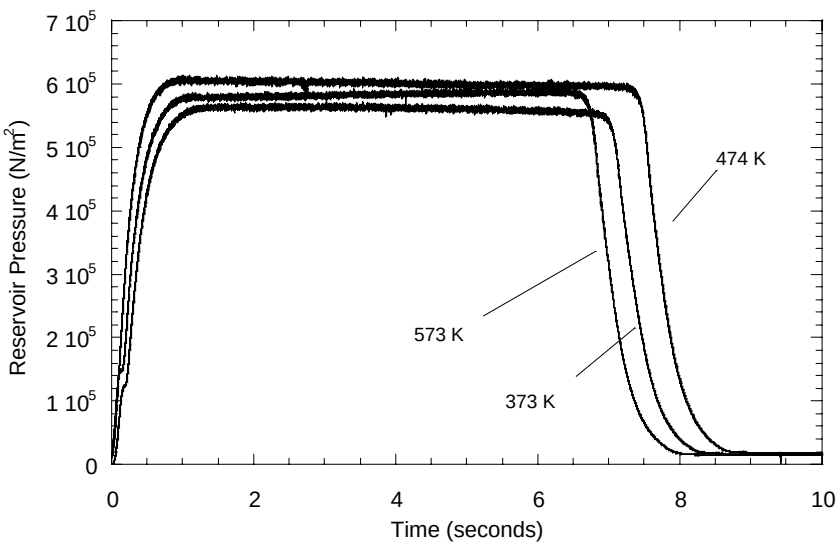

Figure 4: Reservoir pressure

The observed variations in reservoir pressure will lead to variations in pressure within the working section. Figure 5 shows the pitot pressures recorded in the working section. These are recorded simultaneously with the reservoir pressures given in Fig. 4. The series of pressure peaks at the end of the run is due to shocks within the working section during flow shut down.

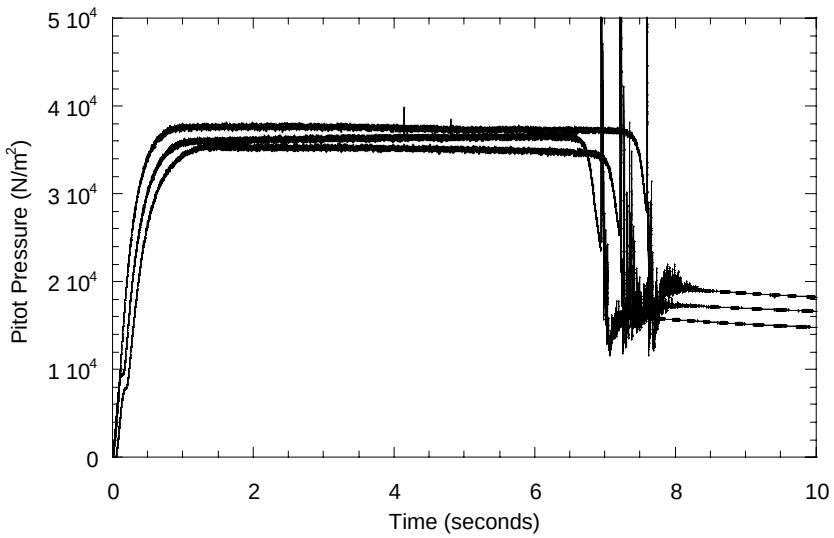

Figure 5: Pitot pressure in working section

The variations in the recorded pitot pressures are seen to be consistent with those recorded in the settling chamber. To provide quantitative results it is necessary to normalise pressures in the working section with those recorded in the settling chamber. Figure 6 shows that the normalised pitot pressure profile remains constant throughout the useful running time and is repeatable from run to run. It is, therefore, possible to eliminate the effect of variation in the pressure measurements caused by the variation in supply pressure.

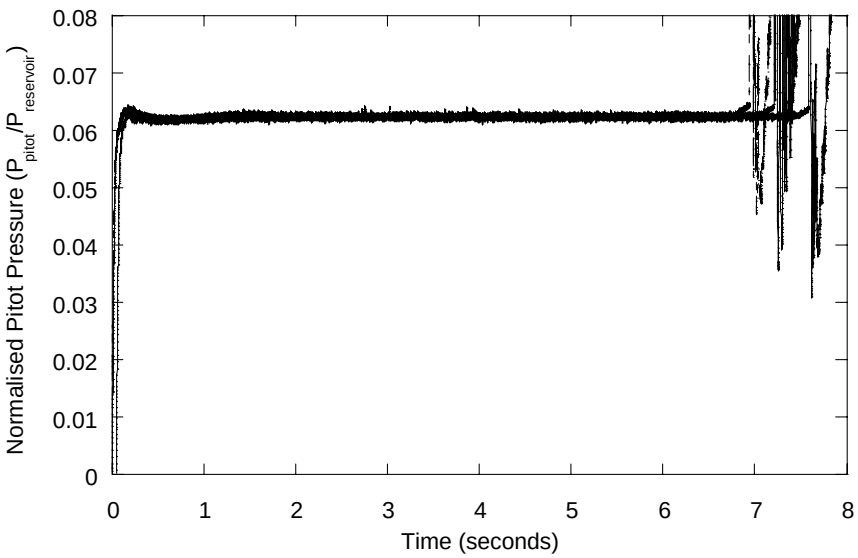

Figure 6: Normalised pitot pressure

As the Mach number in the working section can be obtained from the ratio of the reservoir pressure recorded in the settling chamber and pitot pressure in the working section it can be concluded that the Mach number does not vary throughout the useful running time of the tunnel. That is, the small variation in Reynold's number has negligible influence on the nozzle area ratio through the influence of the displacement thickness of the boundary layers.

For the present study, the following experimental techniques were utilised:

i) A Particle Image Velocimetry (PIV) system was employed to measure the instantaneous two-component planar velocities and velocity vector fields. The resolution of the PIV system close to

the model surface was enhanced with the application of a surface fluorescent paint. The velocities of more than 500 m/s encountered in this flow condition have imposed the use of a double-pulse laser system with a pulse separation time in the microsecond range. The PIV image acquisition system utilises a double-cavity Nd:YAG Litron Laser with a pulse energy of 2 x 200 mJ. The beams are frequency doubled to a wavelength of 532 nm and operated at 15 Hz, with a pulse separation time of 1μs. The scattered light is collected by a 1376*1040 pixel charge coupled device camera (LaVision Imager Intense) and digitized to 12bits. The camera has a maximum frame rate of around 5 image pairs per second. The synchronization between the laser pulses and the camera recording is accomplished by a programmable timing unit embedded in a personal computer dedicated to PIV. A laser light sheet of 0.2 mm in thickness and 160 mm in width at a distance of 5mm and 10mm parallel to the flat plate has been selected. De-agglomerated Aliminium Oxide (Al_2O_3) powder with a manufacturer-specified nominal particle diameter of 300nm and bulk density of approximately 4000 kg/m^3 was used as the seeding element for PIV. The particles were seeded at the settling chamber by means of a high pressure output powder seeder through a tailored made seeding tube. The rotating drum in the seeder dispenses particles at fine sizes and then 6 break-up jets in the powder seeder break up these powder particles into the desired sizes. These jets are driven by compressed air supply at 8bar. The relaxation time of particles is about 5-6 microseconds and a corresponding relaxation length is 4mm. The seeding density of Al_2O_3 was found out to be very good and uniform (compatible with the theoretical seeding density of 10 particles/mm^3). Approximately 20–30 particles were present per interrogation window. The PIV images were processed with a cross-correlation technique using the DaVis7.2 software. In the processing of PIV images, initial interrogation areas were initially selected as 128*128 pixel^2 then refined to 64*64 pixel^2 and a pulse separation time of 1μs enabled particles to move about ¼ of the interrogation window. A 50% overlap was used to provide a vector field of size 40x32 vectors for the small FoV at 10mm away from the plate and 80x64 for the big FoV that is 5mm away from the plate.

ii) Pressure tapings using high sensitivity Kulite pressure transducers (XT-140) were employed to measure surface pressures.

iii) High-speed phase-locked schlieren photography was employed to visualise the flow field.

The experimental setup was designed to be flexible, modular and highly adaptable so as to allow for efficient changeover between the use of different geometries. The model was a zero incidence flat plate with a single sonic jet orifice of exit diameter 2.5 mm which issues normally from the surface into the freestream hypersonic flow, Fig. 7. The flat plate top surface including the jet orifice was made of ceramic material supported by a steel structure. The blunted flat-plate had a hemi-cylindrical leading edge. For the blunted leading edge configuration, the experiments were laminar. For the sharp leading edge configuration, the experiments were turbulent with relatively low/intermediate Reynolds no. which allows the possibility of DNS/LES comparisons. Scalability of the data to higher Reynolds no. will also permit their usage in conjunction with RANS. The plate was instrumented with pressure tappings. Their location is shown Table 1.

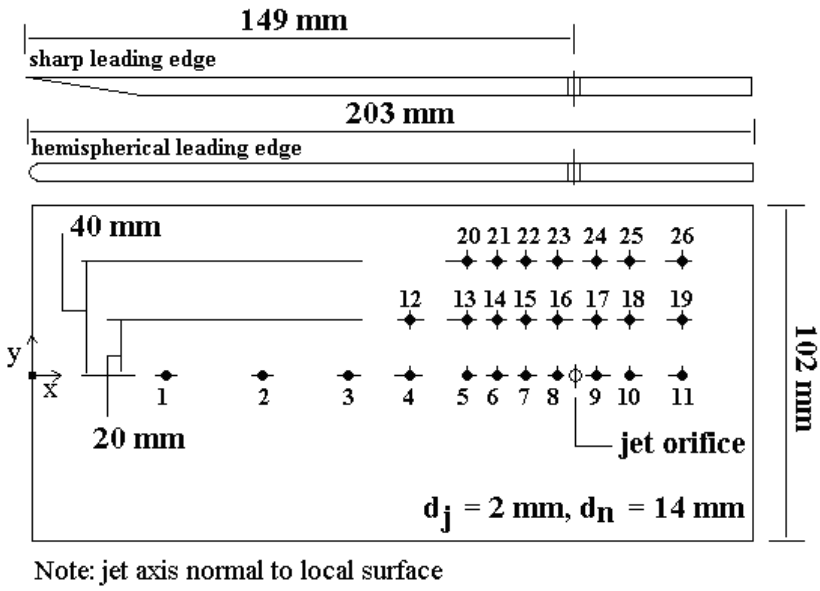

Figure 7: Schematic of flat plate geometry

Table 1 Pressure tappings.

Tapping	x (mm)	y (mm)	Tapping	x (mm)	y (mm)
1	62	0	14	137	20
2	82	0	15	142	20
3	102	0	16	147	20
4	117	0	17	151	20
5	132	0	18	156	20
6	137	0	19	171	20
7	142	0	20	132	40
8	147	0	21	137	40
9	151	0	22	142	40
10	156	0	23	147	40
11	171	0	24	151	40
12	117	20	25	156	40
13	132	20	26	171	40

The non-plasma air jet was fed from an external high pressure reservoir via a plenum chamber contained within the plate, whose pressure was monitored during the tests. The jet flow was controlled by a solenoid valve connected to a timer/sequencer and was synchronised so that it was established just prior to the commencement of the main freestream flow. The plenum chamber remained effectively at room temperature throughout each run.

3. CFD CODE, GRID GENERATION AND VALIDATION

The numerical study employed a three-dimensional, high resolution, iterative, finite volume time marching Navier-Stokes (NS) solver [33]. The region of interest was discretized into small but finite hexahedral cells. The numerical integration procedure produced cell-averaged flow properties, which were assigned to the centres of each face of the hexahedral cells. The Baldwin-Lomax algebraic turbulence model [34] was employed. It has been shown by References 33 and 35, that this turbulence model can successfully calculate separated flows with much more complicated grid geometry than that of the present study. The system of the governing equations has been solved using an explicit Harten-Yee Non-MUSCL (Monotone Upstream-centered Schemes for Conservation Laws) Modified-flux type TVD (Total Variation Diminishing) scheme [36], accurate in time and space. The Roe's average Riemann Solver was used [33], due to its simplicity and its ability to return to the exact solution whenever the

variables lie on a shock or contact discontinuity. The Courant number CFL was chosen as 0.7 to obtain rapid convergence and avoid unsteadiness in calculation. Reference 33 provides a detailed description of the solver. References 33 and 35 provide the validation of the NS solver.
The boundary conditions were non-slip and isothermal. The solution history was monitored and the steady-state solution was selected if the change of the flow field parameters residuals became small. The convergence criterion required that the residuals be smaller than 10^{-5} for the mass, momentum and energy equations. The grid was generated using a three-dimensional transfinite interpolation technique [35], i.e.,
1) Generation of the one-dimensional line grids at all junctions of the domain surfaces with high density at the walls and in the region of the jet, where high gradients exist, to ensure the accuracy of the simulations.
2) Generation of the two-dimensional surface grids for all of the domain boundary surfaces using the one-dimensional line grids as the interpolation boundaries and applying any geometric constraints.
3) Generation of the three-dimensional field grid by interpolation of the surface grids and ensuring the orthogonality of the grid at the wall by specifying the derivative information at the wall occurred. The cluster of the grid at the wall was controlled by either the magnitude of the derivative or the stretch factor in the interpolation. [35]
4) A three-dimensional elliptic smoother was used to smooth the grid in regions where this was critical. The grid points generated were the vertices of the hexahedral cells in the finite volume formulation. A secondary grid was created by the central points of the cells for the presentation of the results from the finite volume solution.
The sensitivity of the numerical solution to the computational grid was checked using five grid densities and distributions. Smoothing and stabilizing parameters were kept to a minimum during the grid-sensitivity studies. The grid was refined in each direction of the three dimensions while holding the other two dimensions fixed. The study showed a difference of less than 1% between results for grid systems of more than 75 nodes in the longitudinal direction, 70 nodes in the vertical direction, and 70 nodes in the lateral direction. A grid system of 80 x 75 x 75 nodes was selected for the present simulations. The minimum grid spacing was 10 μm (in the neighbourhood of the wall), of a typical value of $y+<1$ for the first cell off the body surface for better resolution of the viscous layer.

4. RESULTS AND DISCUSSION

4.1 CLEAN CASE STUDIES

In Fig. 8, the averaged instantaneous PIV vector fields for the three different cases, Case 1 (373K), 2 (474K) and 3 (573K), are plotted in terms of average and Root Mean Square (RMS) - flow is from right to left. These cases correspond to a distance of 10mm from the plate. The maximum in plane velocity observed is approximately 490, 430 and 500 m/s respectively for the three cases. RMS values are within similar range for Case 1 and Case 3 nonetheless they are well above for Case 2. The direction of RMS vector remains unchanged between cases even though the mean velocity shows some variation. However, data analysis identified the presence of low frequency coherent structures, and indicated that the global flow features and low frequency motion inside the boundary layer are Reynolds no. dependent. Further studies are currently under way to improve S/N, to optimize seeding quality and uniformity, and to determine the effect of seeding on the flow properties inside the settling chamber and test section. Detailed time resolved surface pressure and Pressure Sensitive Paint measurements are under way to shed further light into the observed phenomena.

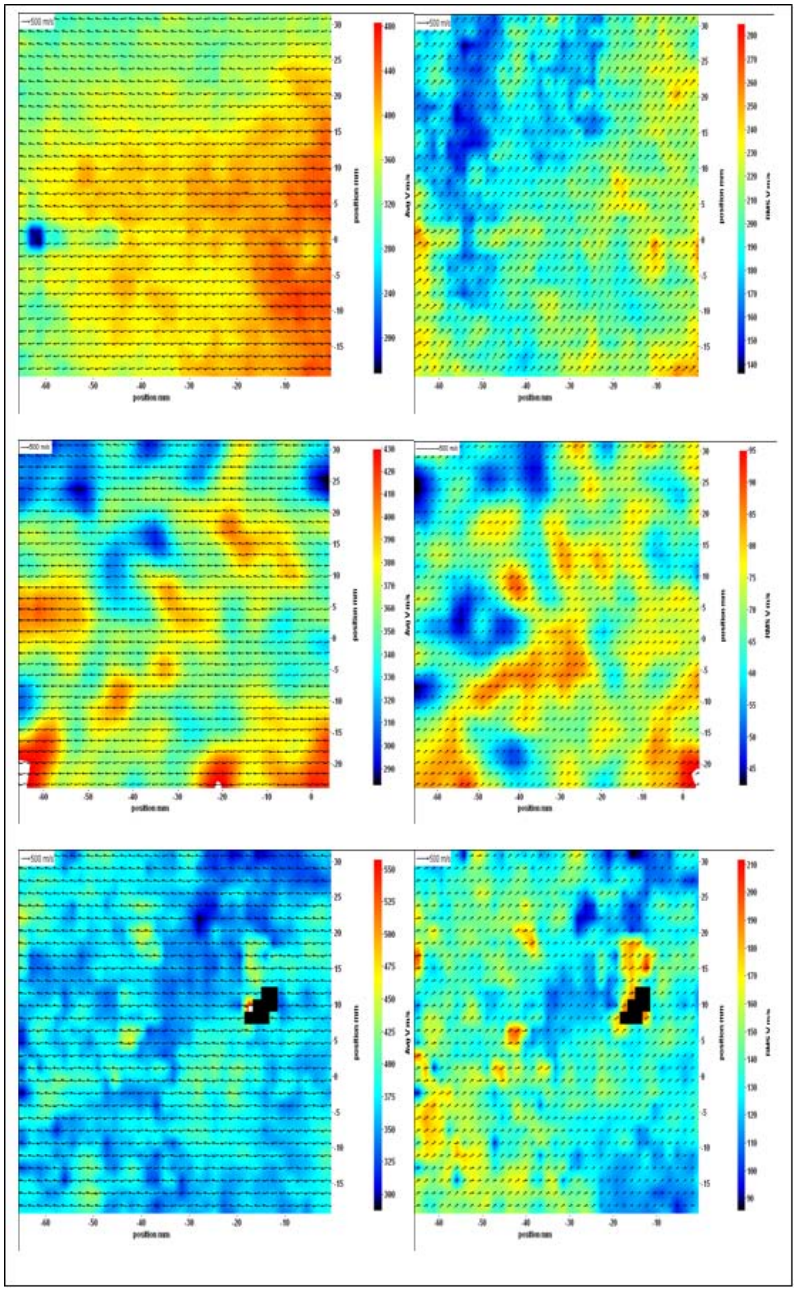

Figure 8: Average and rms velocities for Cases 1, 2 and 3

4.2 BASELINE TRANSVERSE NON-PLASMA JET INTERACTION STUDIES

Figures 9 and 10 show the typical jet flow field interaction obtained using the schlieren method together with a schematic diagram explaining in detail the observed flow phenomena. The experiments were conducted with a sonic under expanded jet ($P_{oj}\approx 7.5\times10^5$ Pa, $P_{oj}/P_\infty\approx 700$). The jet plume presents an obstacle to the external flow, Fig. 9, which causes a strong shock, which causes the boundary layer upstream of the jet to separate. In contrast to the two-dimensional situation in which the entire external flow must go over the jet-induced obstruction, the flow can go around the three-dimensional jet. The flow field near the separation point is controlled by the interaction between the resultant free shear layer and the external stream. As a result of high pressures downstream of the separation shock and mixing between the two streams, the jet is turned in the direction of the external flow, Fig. 9. A three-dimensional shock structure forms in the jet plume as it is turned, bounded by a three-dimensional mixing layer. Some of the high-pressure external air behind this separation shock flows downstream, causing a high-pressure region in front of the jet. From this high-pressure region, the external air also flows radially outward along the surface of the plate, expanding to lower pressures. Finally, this expanding reverse flow is terminated by a shock system. As the reverse flow continues outward from the jet, it turns toward the downstream direction. To satisfy the boundary conditions, at least two counter-rotating vortices must be present within the upstream separated region, Fig. 10, the

clockwise separation vortex in the separated flow region and the counter clockwise jet horseshoe vortex in the region immediately upstream of the jet. An important feature of interest is the strong shock, which terminates the supersonic region of the jet (often referred to as the Mach disk or normal shock). The Mach disk is dish shaped and parallel to the exit plane, Figs. 9 and 10.

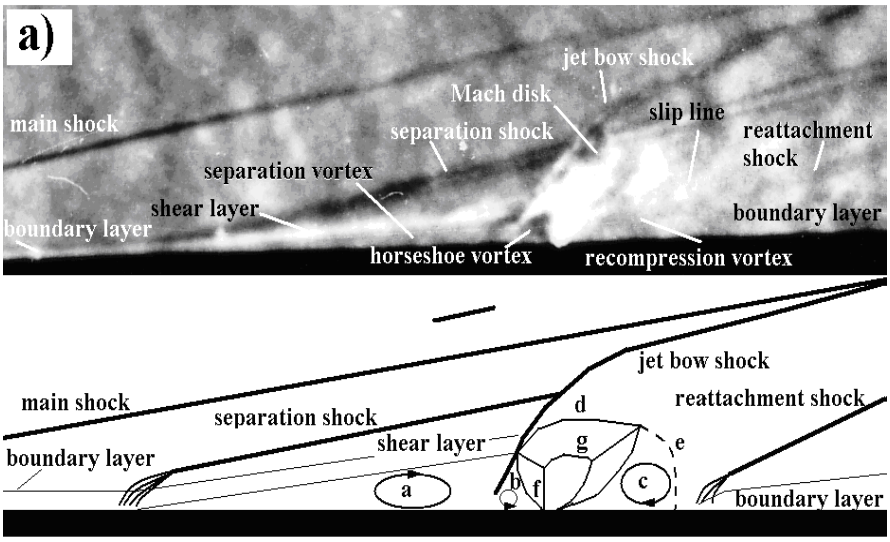

a, separation vortex; b, horseshoe vortex; c, recompression vortex;
d, Mach disk; e, slip line; f, jet boundary; g, internal shocks.

Figure 9: General structure of the interaction region for the sharp plate at α=0 deg.

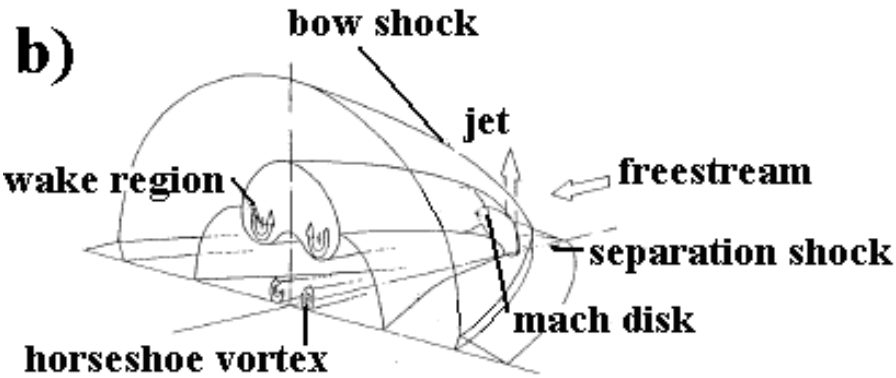

Figure 10: Three-dimensional jet flow structure.

4.3 PRESSURE MEASUREMENTS

The pressure distributions in the interaction region show a repeatability of ±5%, Fig. 11. Separation was taken to be at the midpoint between the plate pressure and the plateau pressure levels. The location correlates well with schlieren observations of the location of the separation shock. The pressure along the plate centreline increases to the point at which flow separates, and then there is a further rise to a pressure plateau. In the vicinity of the jet, the pressure distribution shows a small drop from the plateau value. After this drop, the pressure rises to a peak just ahead of the jet. The position of this peak corresponds with the location of the main reattachment ahead of the jet. The scaling of the separation length based on the local Mach number, jet diameter and the jet to local undisturbed pressure ratio is shown in Fig. 12. The data correlates as

$$\frac{L_{sep} M_2^{5/2}}{d_j} = 5\left[\frac{P_{oj}}{P_2}\right]^{8/7} \qquad \ldots(1)$$

The correlation suggests that the length of the separated flow region increases with an increase in the jet to undisturbed flow surface value pressure ratio and a decrease in the local Mach number ahead the separation. The range of variables was limited and more data are required.
For a blunt flat plate at incidence, the local Mach number ahead of the jet-induced separation region was calculated using the Rayleigh-pitot relationship assuming the flow at the edge of the boundary layer to be isentropic using the measured undisturbed pressure P_2. For a sharp flat plate at incidence, the local Mach number was calculated using the oblique shock in a perfect gas data tables.

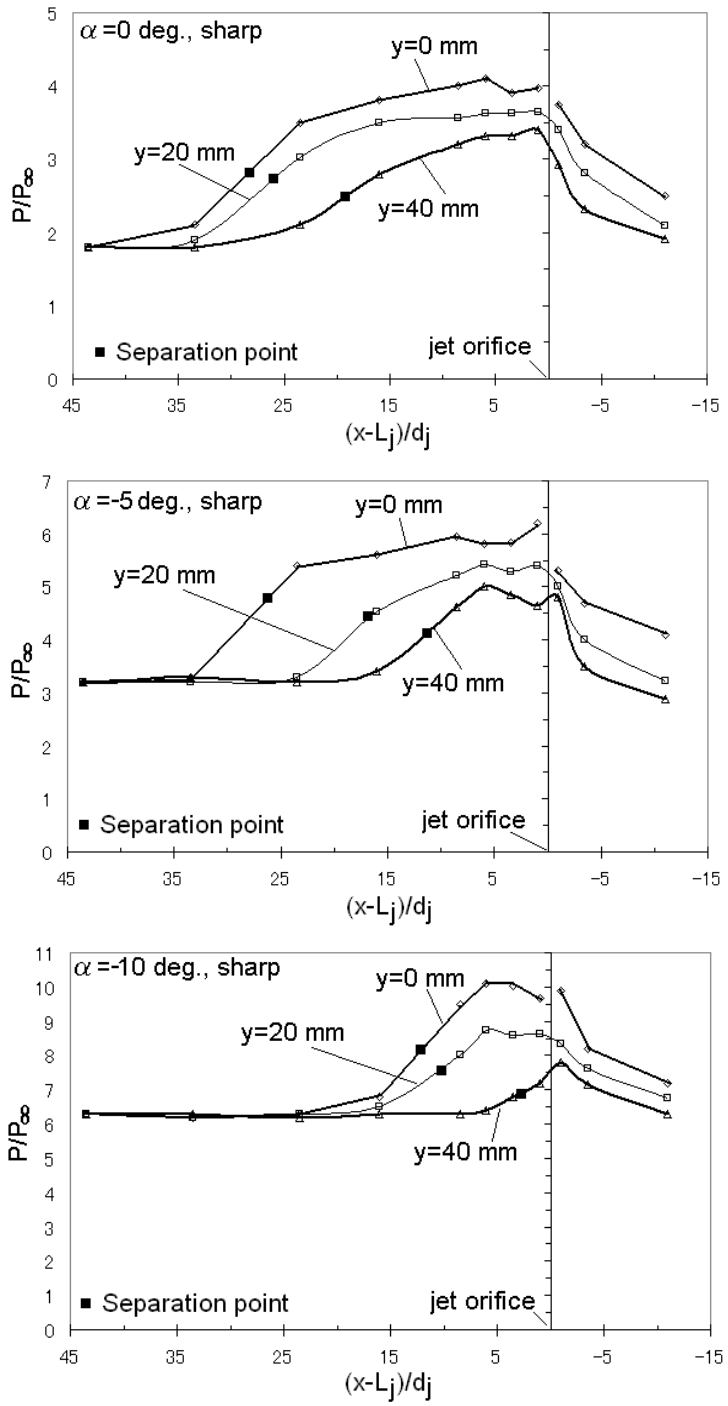

a) Sharp flat plate.

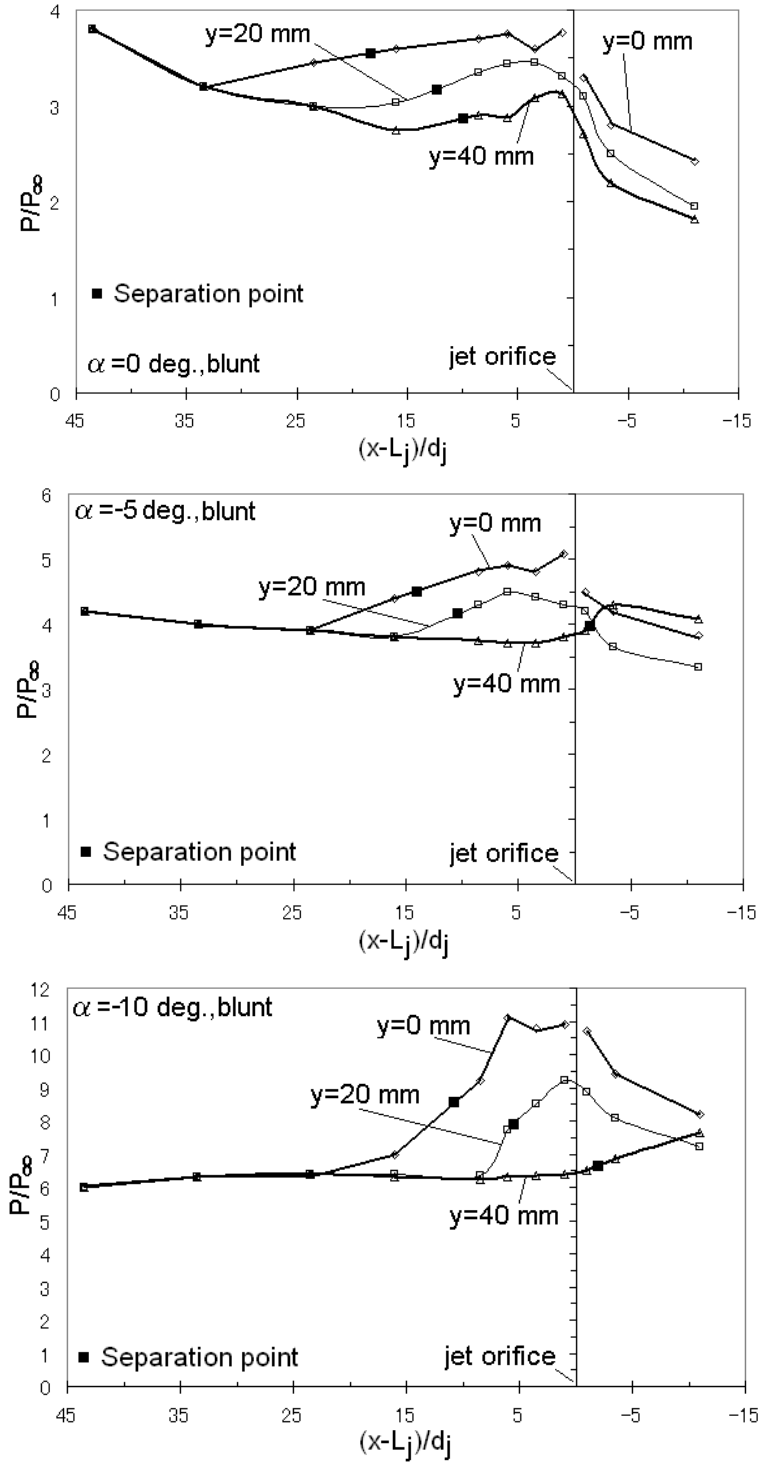

b) Blunt flat plate.

Figure 11: Pressure distributions.

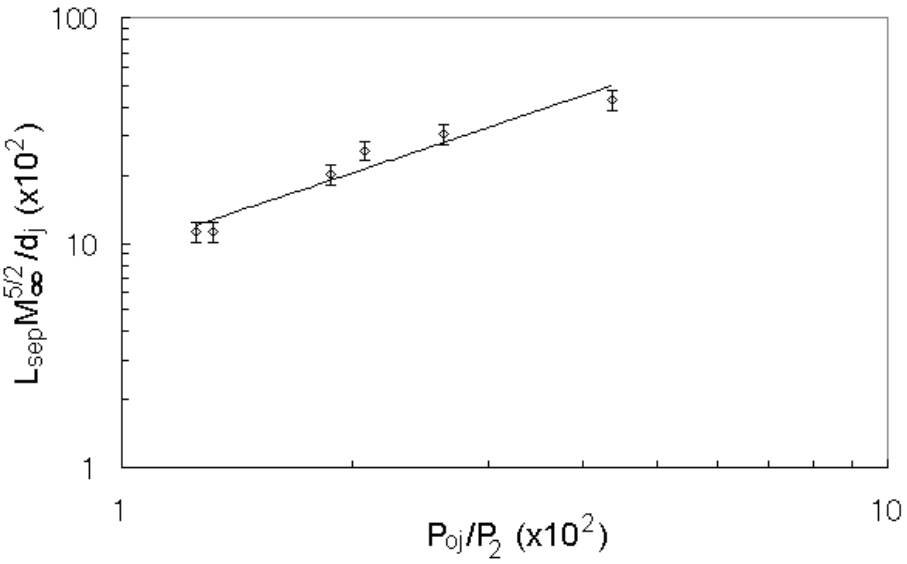

Figure 12: Correlation of the separated flow length along the plate centreline.

4.4 ANALYTICAL PREDICTION OF SEPARATION LATERAL SPREADING

The shape of the separation front around a circular jet on a flat plate is a function of the shape of the bow shock,

$$\frac{R_{sep}}{d_j} = H\left(\frac{P_{oj}}{P_2}\right)^{1/4}\left(\frac{\psi}{d_j}\right)^{1/2} \qquad \text{…(2)}$$

where

$$H = \left[\frac{1.14\gamma}{M_2}\left(\frac{2}{\gamma+1}\right)^{\frac{\gamma+1}{2(\gamma-1)}}\left(1+\frac{\gamma-1}{2}M_2^2\right)^{\left(\frac{\gamma-1}{\gamma}\right)+\left(\frac{\gamma+1}{2(\gamma-1)}\right)}\right]^{1/4}$$

Using Eq. (2), the shape of the associated separation front can be written as,

$$\frac{R_{sep}}{d_j} = H\left(\frac{P_{oj}}{P_2}\right)^{1/4}\left(\frac{x-x_{sep}}{d_j}\right)^{1/2} \qquad \text{…(3)}$$

As it was discussed in section 4.3, the separation length data directly upstream of a jet along the centre line of a plate passing through the jet correlates as,

$$\frac{x_{sep}}{d_j} = \frac{L_j}{d_j} - \frac{5}{M_2^{5/2}}\left(\frac{P_{oj}}{P_2}\right)^{8/7} \qquad \text{…(4)}$$

Substituting Eq. (4) into Eq. (3) then,

$$\frac{R_{sep}}{d_j} = H\left(\frac{P_{oj}}{P_2}\right)^{1/4}\left[\frac{x-L_j}{d_j} + \frac{5}{M_2^{5/2}}\left(\frac{P_{oj}}{P_2}\right)^{8/7}\right]^{1/2} \qquad \text{…(5)}$$

where L_j represents the x-direction location of the jet hole.

In Fig. 13, the predictions from the algorithm of Eq. 5 are compared with experimental measurements using pressure tapings and computational simulation results using the CFD code described in section 3. The agreement between the experimental and predicted (Eq. 5) locations of the separation front is within ±6%, whereas the agreement between the experimental and predicted (CFD) locations is within ±2%. The predictions of Eq. 5 are independent of Reynolds number effects.

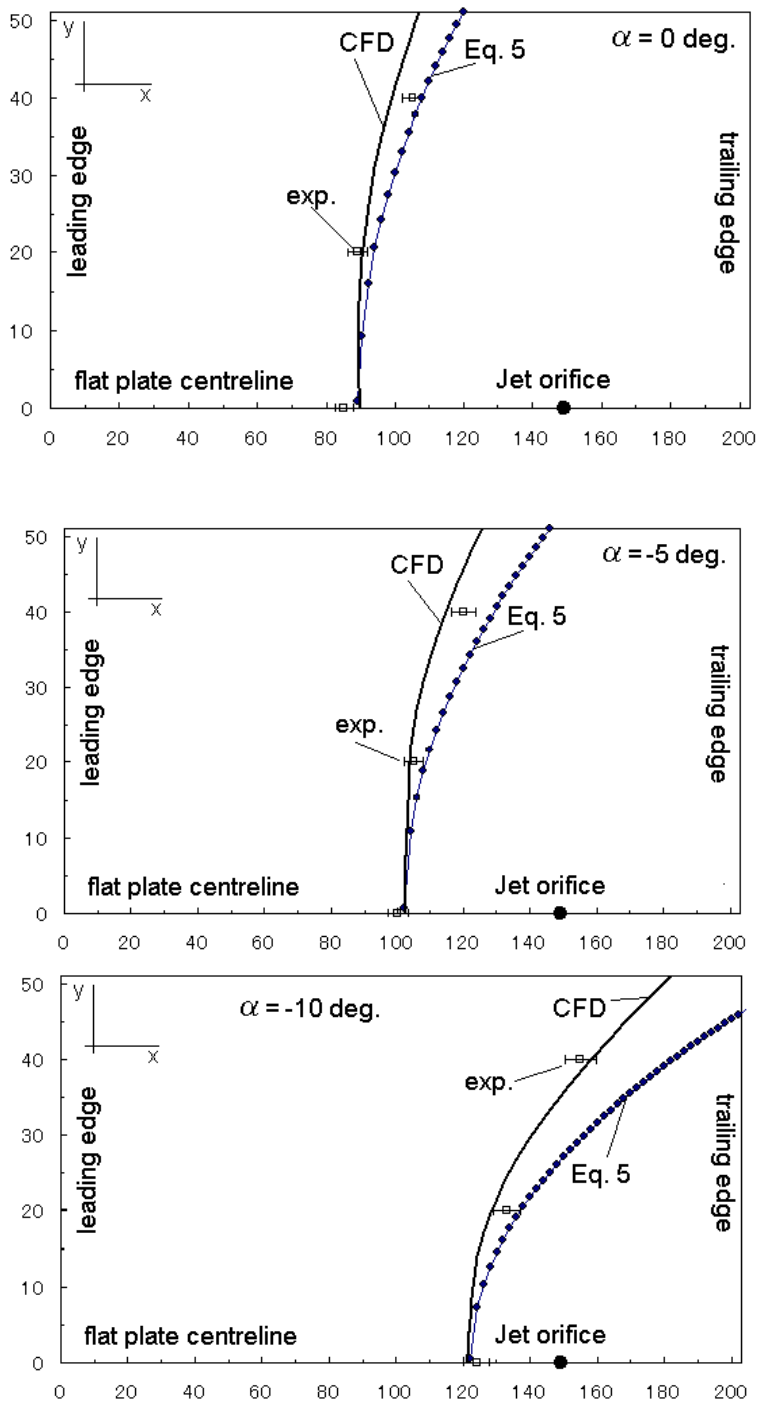

a) Sharp flat plate.

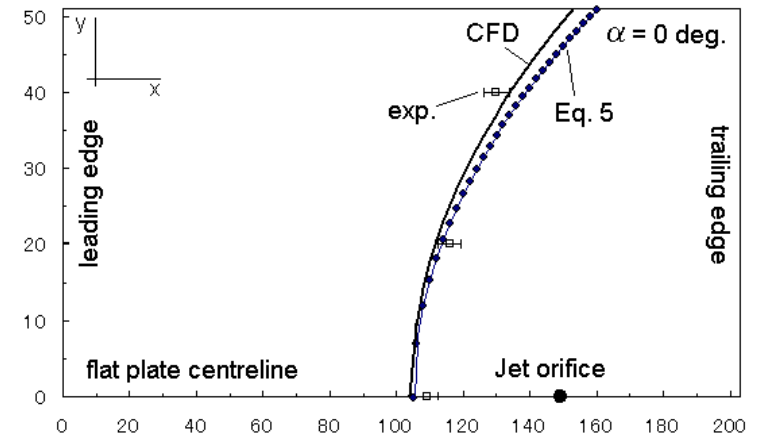

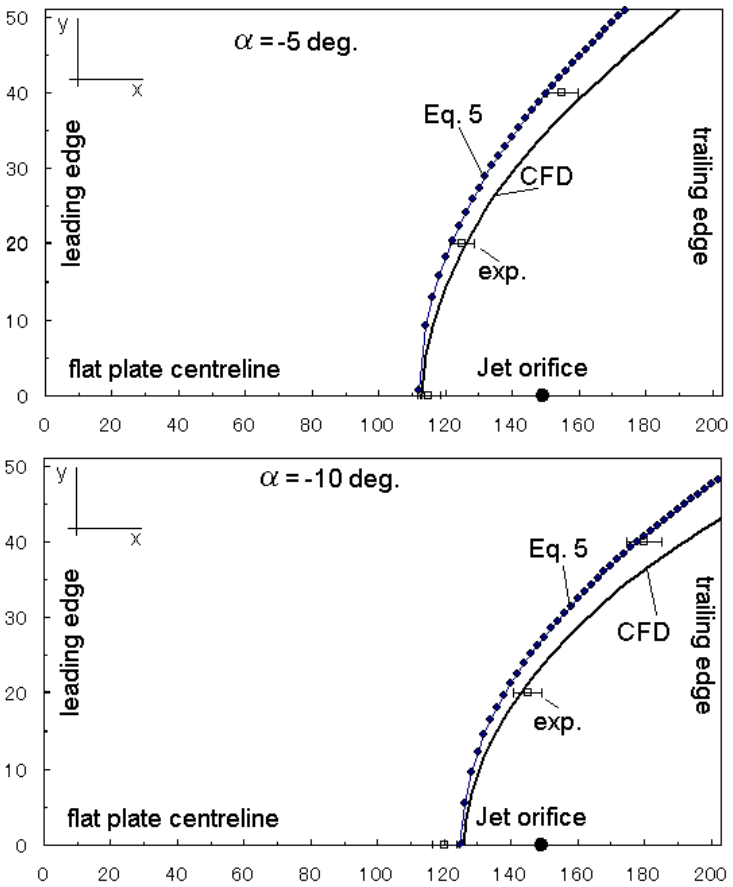

b) Blunt flat plate.

Figure 13: Comparison of the predicted (Eq.5 and CFD) and measured separation fronts.

4.5 ANALYTICAL PREDICTION OF JET PENETRATION HEIGHT

The schlieren pictures of the shock patterns produced by the jet injection are reminiscent of the flow around a cylinder protruding from a solid surface. Based on this analogy, the modified equation of Zukoski and Spaid [36] was used, where the pressure coefficient corresponds to the stagnation pressure of the equivalent cylinder protruding behind a normal shock in the primary flow of Mach number M_2. Two assumptions were made; the jet interaction resembles (i) that of a quarter-sphere-half-cylinder model, and (ii) that of a spherical nosed cylinder. Figure 14 shows that assumption (ii) seems to agree better with the experimental findings of the blunt plate, whereas assumption (i) seems to agree better with the experimental findings of the sharp plate. This is some indication of the different shape of disturbance.

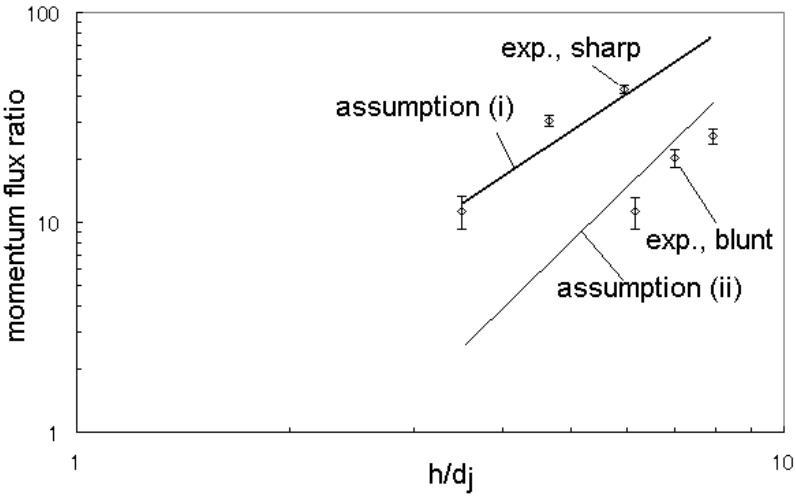

Figure 14: Correlation of jet penetration heights.

4.6 EFFECT OF BLUNTNESS

Figure 15 shows that the introduction of leading edge bluntness, although it effectively increases the jet by reducing the local surface pressure ahead of the separation region, causes a delay in separation. Bluntness causes the boundary layer to grow by mutual interaction with the entropy layer. The boundary layer pressure gradient of the flat-plate remains positive. Bluntness increases the magnitude of the pressure gradient upstream of the jet and, consequently, causes the velocity distribution in the boundary layer to be fuller, i.e. more positive, close to the surface of the flat-plate. The reduced lengths of the separated regions are also evident from the pressure distributions, Fig. 11.

The whole flow field is influenced by the entropy layer. The boundary-layer edge becomes totally invisible for the blunt plate. This is because the highly curved shock wave produces strong density gradients throughout the entire flow field that obscure the density gradients in the boundary layer, thus making the identification of separation of the flow very difficult. The pressure measurements at zero incidence without jet, Fig. 11, show that the effect of the leading edge bluntness is felt over the entire body length. The surface pressure distribution is reduced by the expansion at the shoulder to about 70% of the sharp plate values. Because of the lower undisturbed surface pressure on the blunt plate, the jet pressure ratio P_{oj}/P_2 is higher on the blunt plate than on the sharp plate and, therefore, the jet penetration into the undisturbed flow will be greater in the blunt plate case, Fig. 14. The difference between the two plates reduces as incidence decreases. This is because the bluntness effect on surface pressure distribution diminishes and approaches the equivalent sharp plate surface pressure near the jet as the angle of attack decreases. The jet bow shock is closer to the jet for the sharp configuration, e.g., Fig. 15; this is due to the higher total pressure in the shock layer and the higher local stream velocity (as the local surface Mach number is higher than for the blunt plate case).

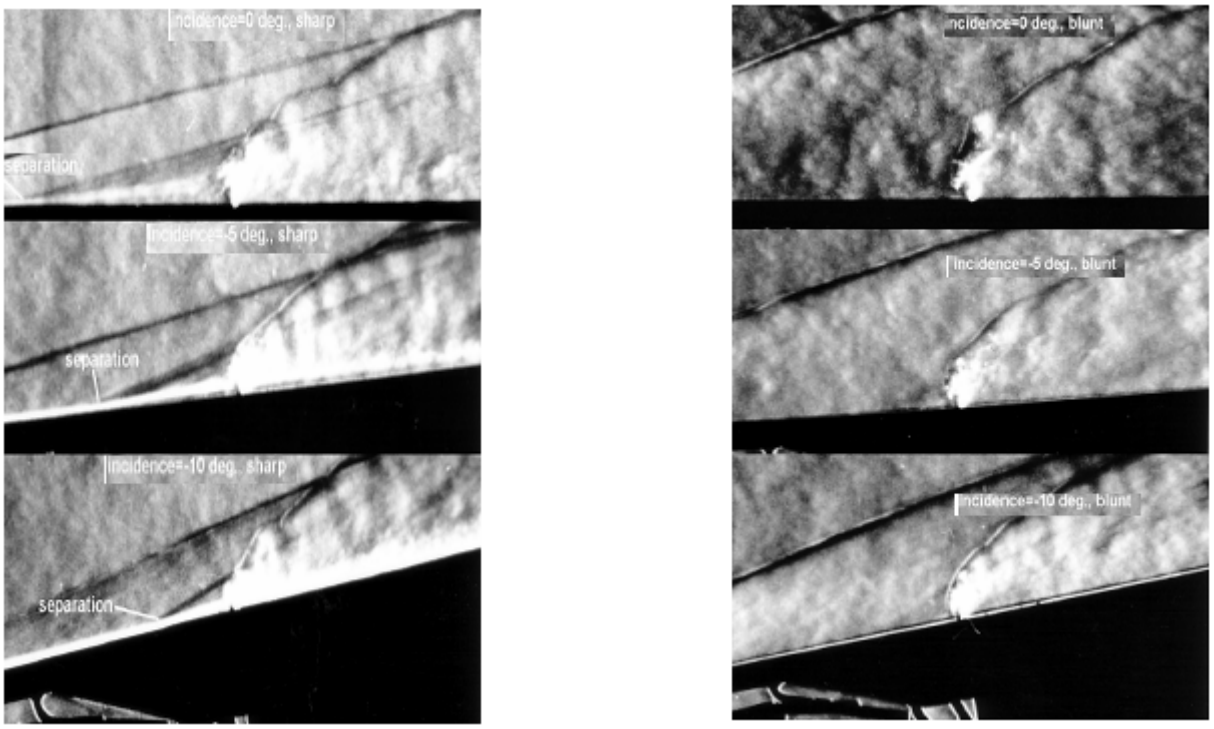

a) sharp plate b) Blunt plate

Figure 15: Schlieren visualization studies.

5. PLASMA ACTUATOR SYSTEM

In recent years, there has been a considerable interest in the use of electric discharge plasmas for flow control. Engineering applications of the plasma-assisted flow control mainly focus on viscous drag reduction and control of boundary layer separation in low-speed flows, shock wave modification and wave drag reduction in supersonic and hypersonic flows, as well as supersonic boundary layer transition control. In summary, electrohydrodynamic (EHD) flow control is

feasible only in low-speed flows, magnetohydrodynamic (MHD) interaction is feasible only in low pressure flows, and most thermal flow control methods require very high plasma/laser power budget. Samimy et al [37] have developed localized arc filament actuators to control high speed and high Reynolds number free jets. At the present time, the localized arc plasma approach, remains the only energy efficient, high-speed, high static pressure flow control method demonstrated in well characterized experiments. The mechanism of the flow control by the present method is generation of perturbations of high amplitude and high frequency to excite flow instabilities in high-speed and high Reynolds number flows by using localized, rapid heating of multiple small areas of the flow by arc discharges (arc plasma actuators) located in the region of maximum flow receptivity (i.e. near the exit place of a nozzle). The key benefit of localized arc plasma actuators, compared to mechanical and acoustic actuators, is that they uniquely combine wide range of operation frequencies (0 to 200 kHz) with large forcing amplitude. The multiple arc plasma actuators can be independently controlled by varying the repetition rate, duty cycle, and phase. This makes it possible to trigger and amplify specific flow instabilities, such as jet column instability, shear layer instability, and various modes of these instabilities. For this reason, significant flow field changes can be produced at relatively small energy cost for operating plasma actuators.

In the present research, the LAFPA approach to enhance mixing of the cross-flow jet interaction through modification of instabilities is utilised. The LAFPA system is based on the design of Samimy el al [37], see Figure 16. The actuators are operated by an electronic input signal, which makes them ideal for both open and closed loop active flow control.

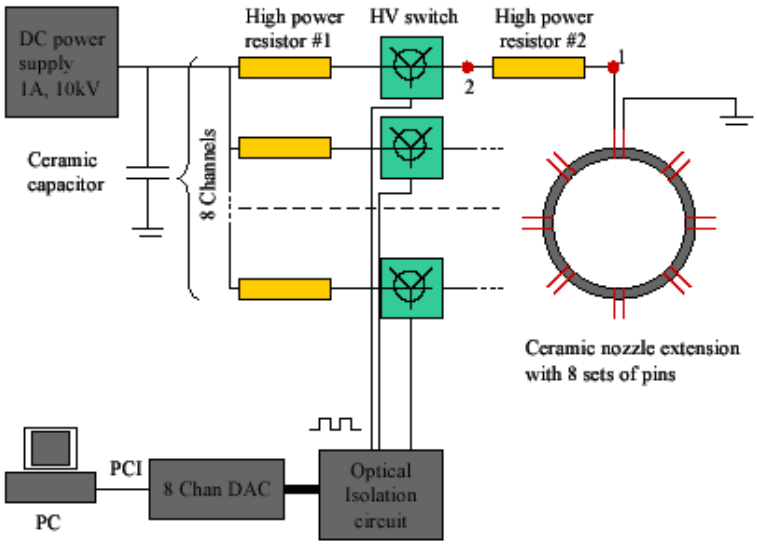

Figure 16: Schematic of the LAFPA system.

Figure 17 shows the picture and schematic of the manufactured plasma generation system. The device can be used to generate powerful high frequency pulses with a duration of up to 300 μs. The device is operational from 230V AC grid power supply voltage. The device consists of a power factor controller, which converts the 230V AC to 400V DC, a control/driver board, which generates externally controlled HF burst pulses with a frequency adjustable around 1 MHz, a full bridge converter for pulsed operation, which can operate in the frequency range of 800-1100 kHz, and an output transformer cascade which transforms the voltage to up to 76 kVpp. The burst pulses of the pulse control board are controlled by a TTL input (BNC connector). The generator is adjusted such that it should reach its design parameters at 1 MHz. Frequency adjustment is the primary means of adjustment of the generator as it also adjusts amplitude. The system is fully controlled by an National Instruments data acquisition and control system using an in-house developed software.

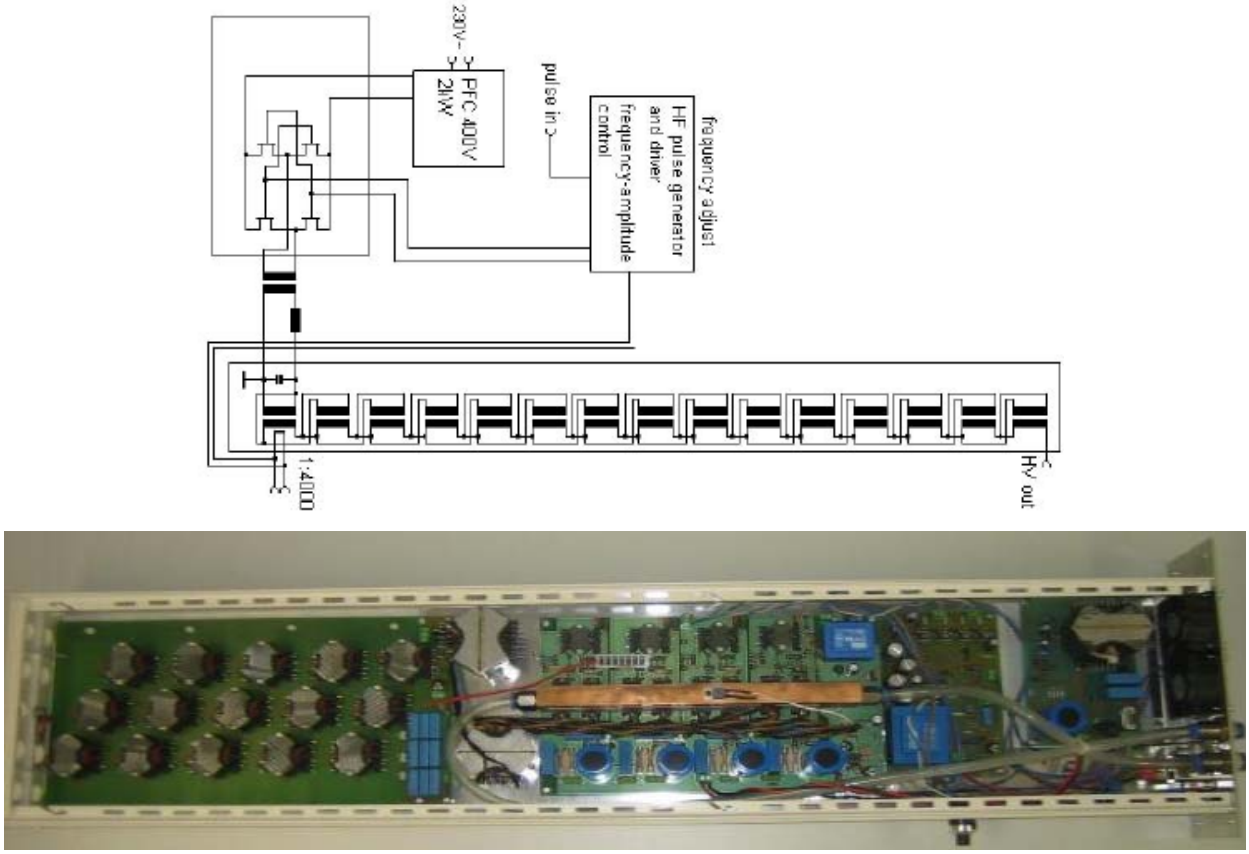

Figure 17: Plasma generation system.

Two nozzle inserts were designed and manufactured made of boron nitride, which has high electrical resistance and density, and low porosity. The convergence sonic nozzle is shown in Fig. 18a, and the convergent-divergent supersonic (M=1.3) nozzle is shown in Fig. 18b. Both nozzles are instrumented with tungsten wires connected to the plasma generation system described in Fig. 17.

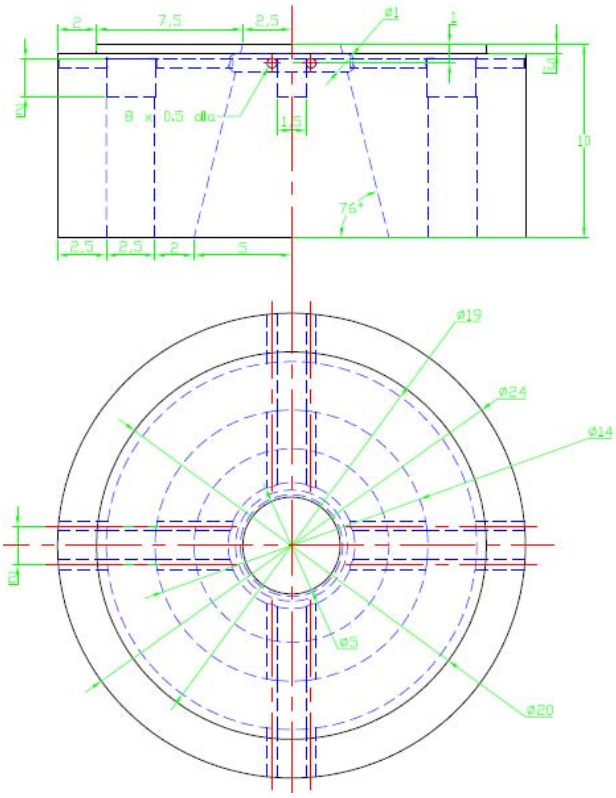

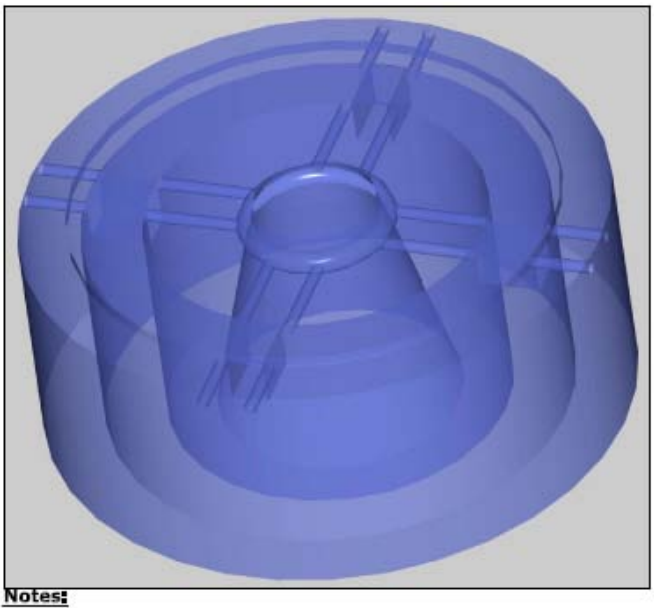

Notes:

All in mm.

The holes (8 of them with 0.5mm diameter) emerging from 1mm diameter groove, start at 1mm below top.

The groove starts at 1mm below top.

Figure 18a: Sonic nozzle.

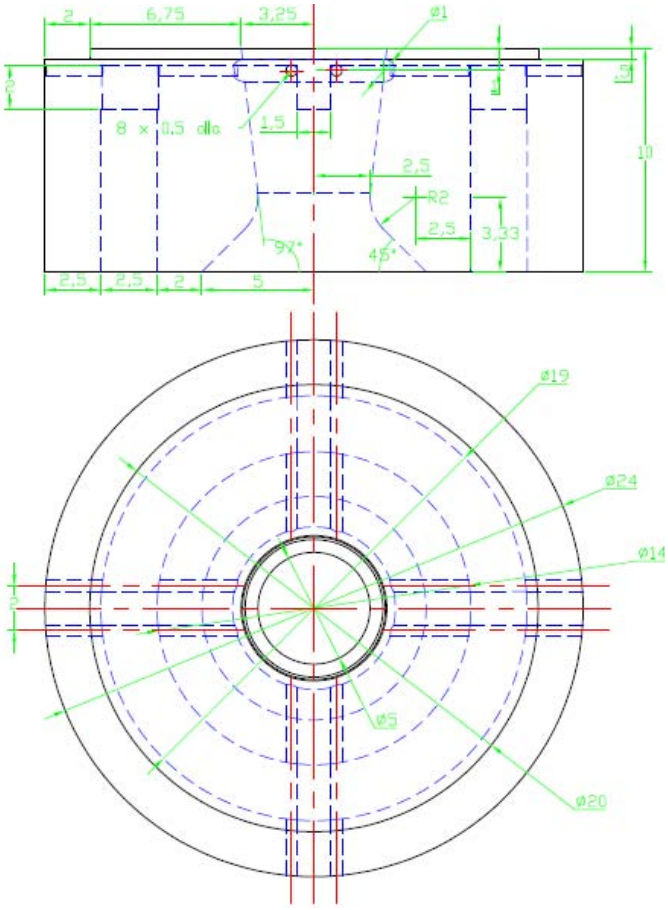

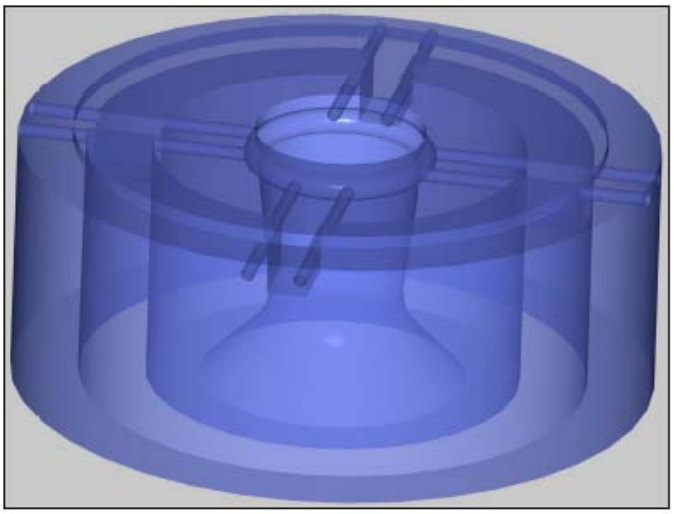

Notes:

All in mm.

The holes (8 of them with 0.5mm diameter) emerging from 1mm diameter groove, start at 1mm below top.

The groove starts at 1mm below top.

Figure 18b: M=1.3 nozzle.

6. PSP SYSTEM VALIDATION

The Pressure-Sensitive Paint (PSP) technique offers the advantage of non-intrusive global mapping of the surface pressure, [38-39]. Using a PSP obtained from McDonnell Douglas Aerospace (MDA PF2B), Taghavi et al., 2002 and 1999, obtained pressure data for a multi-jet supersonic ejector and were able to capture key flow properties such as bubbles of separated flow, and the shock cells within the flow and hence, confirmed the efficacy of the aforementioned PSP formulation. Huang et al., 2007, used PSP to study shock structures on the micro-scale. The PSP formulation developed in-house at the Aero-Physics Laboratory, exhibits relatively low temperature sensitivity which has always been an intrinsic drawback of the PSP technique, forcing researchers to use a combination of PSP along with a Temperature Sensitive Paint (TSP) or numerous temperature sensors to correct for temperature variations along the model surface (Taghavi et al., 2002). Combined with the *in-situ* calibration procedure we aim to provide an accurate measurement of the surface pressure in a two-dimensional supersonic jet system. The presented experiments aim to validate the PSP system for high speed jet applications.

Methyl triethoxysilane (MTEOS) was used as the sol-gel precursor since under optimum conditions it creates a smooth coating with good adhesion (Basu 2007). Ruthenium bathophenanthroline perchlorate was chosen as the luminophore as it has been repeatedly demonstrated to exhibit significant oxygen sensitivity in its luminescence (Tang, et al., 2003, O'keeffe et al., 1995). The formulation consisted of: Ruthenium, MTEOS, ethanol and hydrochloric acid (0.1M).

Setup

A-priori calibration was employed to determine the pressure sensitivity of the PSP formulation. This was carried out in a pressure/temperature controlled chamber where the pressure was varied between *0* and *4.5 bar* and the temperature could be controlled between *270K* and *330K*. The temperature of the paint sample was controlled using a Peltier heater/cooler and monitored by a thermocouple. The peltier heater used for calibration purposes was manufactured by *Greenweld*. The heater was capable of producing sub-zero temperatures as low as *258 K*, with a maximum working temperature of *343 K*, the dimensions were *30 × 30 × 4.7 mm*. An aluminum test sample measuring approximately *30 × 30 × 3 mm* was initially spray coated with *2-3* layers of matte white paint *24 hours* prior to the application of the PSP and allowed to dry.

Once the sample was ready it was spray-coated with *9* layers of PSP and cured at a *343 K* for *7 hours*.
The sample was illuminated by a pair of LED arrays with a peak wavelength of $\lambda = 470nm$, and the luminescent emission was captured by a camera (LaVision Image Intense). A pair of LED panels were employed so that in any setup the camera could be positioned normal to the test section with an LED panel exciting the PSP from each side, leading to uniform illumination. The main advantage of placing the camera normal to the test section is that it reduces the danger of surface contamination due to internal reflections. A combination of two filters was used to capture the emitted light. The first, an orange long-pass filter, only allowing the transmission of light with $\lambda > 600\ nm$ and the second filter was an Infra-Red (IR) cut-off filter, preventing the transmission of light with $\lambda < 700\ nm$. From the plot of I_{ref}/I vs. P/P_{ref}, where I_{ref} and P_{ref} correspond to the no flow state, the pressure sensitivity of the paint defined as $PS = \Delta(I_{ref}/I)/\Delta(P/P_{ref})$ was determined. This plot, commonly known as the Stern-Volmer plot, is presented in Fig. 19.

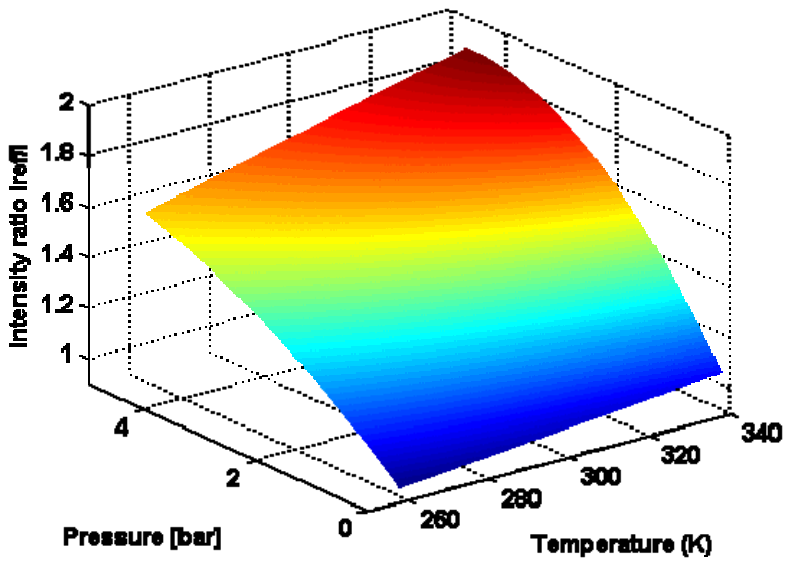

Figure 19: Stern-Volmer plot.

By taking the ratio of wind-off (I_{ref}) to wind-on (I), the effect of paint thickness and luminophore concentration could be eliminated. The temperature sensitivity of the PSP for different pressures tested is presented in Fig. 20. The maximum temperature sensitivity of the paint ($(\Delta I_{ref}/I)/\ \Delta T$) was estimated as 0.46%/^{o}K. The temperature sensitivity of the PSP formulation used in the current investigation is smaller than the PSP recipe of the University of Washington and also that of the Arnold Engineering Development Centre (AEDC) (Moshasrov et al., 1998).

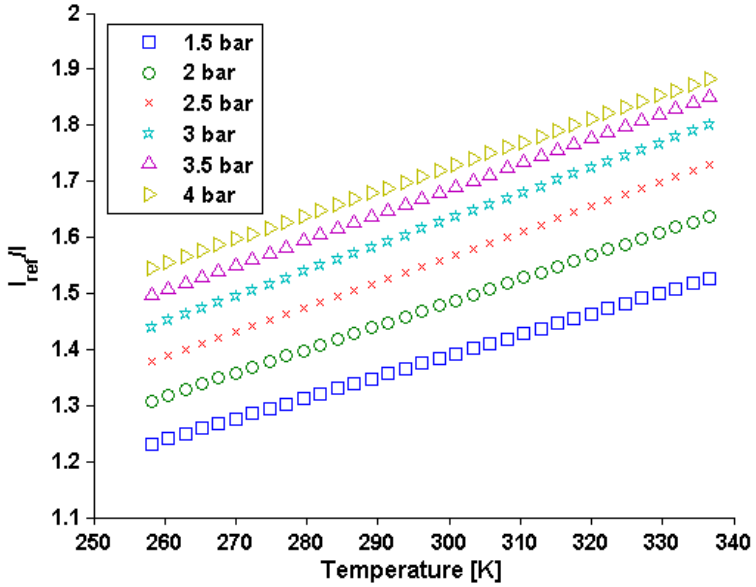

Figure 20: Temperature sensitivity of PSP at various pressures.

Nozzle

The nozzle shown in Fig. 21 was cut from the same piece of steel. This material was used because it has uniform thickness, nominally *19.05 mm*, and is stress free and, therefore, does not warp when cut (Eustace 1969). The nozzle has a contraction ratio of *6:1* and a throat height of *9.6 mm*. The ejector (mixing tube) side walls were milled to shape and are bolted directly to the outer frame. The ejector side walls become parallel to the centre line at the plane of the nozzle exit with a distance of *45 mm* between the upper and lower walls. The total length of the test section was 307 *mm* with a height of *209 mm*. For the PSP experiments, one side of the nozzle is covered using an aluminum plate coated with the PSP while the other side is covered with optical grade perspex.

To provide a good seal between the test section and the two joining side walls a thin layer of the *Hermatite* instant gasket was applied. Since the seal is very flexible, when the side walls are screwed on it has negligible thickness. This provides a good seal for high pressures and because it is only a very thin layer it does not alter the thickness of the test section, ensuring a truly two-dimensional geometry. A rubber gasket was also thought to be used but because of the very delicate shape and thickness of the nozzle, especially at the exit of the convergent section, this idea was not approved. Figure 21 also shows the location of the pressure tappings on the side wall, marked out with black squares.

The plate coated with PSP was initially covered with *2 - 3* layers of primer to give a uniform background. Matte white paint was used as the primer. The plate was allowed to dry. Afterwards, the PSP was spray-painted using an air-brush and the plate was heat treated at *343K* for approximately *7 hours*. This procedure is identical to the preparation of the sample used for *a-priori* calibration. Once the plate was ready it was fastened on to the nozzle with screws and the side with the perspex was covered with a black piece of cardboard to cut out any light shining on the PSP surface with the exception of just before and during image acquisition to reduce effects of photodegradation. The exposure time was *0.9 seconds.*

The inlet pressure was varied between the range *1.2-3.0 bar*, with ambient pressure taken as *1 bar*. This corresponds to a fully expanded Mach number range $0.52 \leq M_j \leq 1.36$ (White, 2003). The "fully expanded Mach number," M_j, is the ideal Mach number achievable by isentropically expanding the plenum pressure to the ambient value. For each pressure setting a wind-off image was obtained just before and immediately after the flow was introduced and the average of the two wind-offs was used as I_{ref}. Using the average wind-off image reduces bias errors due to long-term drift in the voltage out of the measurement system caused by changes in illumination intensity and photo-degradation of the PSP luminophores (Raju and Viswanath, (2005) and Carroll et al., (1996)).

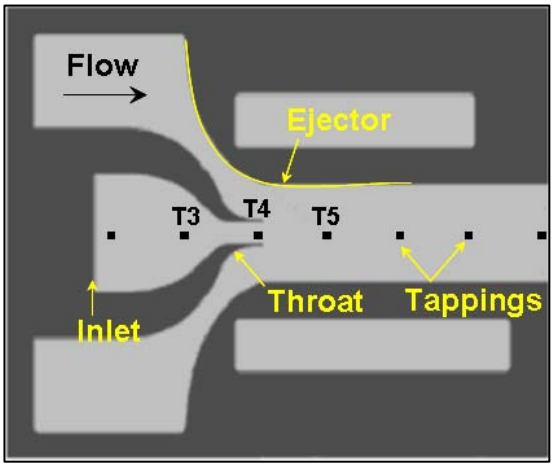

Figure 21: Schematic of test section.

Results

The *in-situ* calibration was applied to the experimental results of steady flow through the nozzle. The benefit of *in-situ* calibration is that it eliminates the dependency of the Stern-Volmer constants, obtained from *a-priori* calibration, to the setup. This involves the location of the different apparatus, such as the camera and light source, relative to each other. It is believed that the effects of temperature changes were minimized by the use of *in-situ* calibration using the wall static taps. This is because the model surface temperature is different during the wind-off and wind-on cases; therefore, the intensities obtained during an experimental run provide a more accurate means of calibration since the intensities take into account the changes in surface temperature (Liu and Sullivan 2003, Taghavi et al., 2002). Pressures obtained from transducer 2 (T2 in Fig. 21) were used for in-situ calibration, since it recorded the largest variation in pressure and would therefore provide a better curve fit.

To examine the accuracy of the results PSP results, simultaneous pressure measurements were conducted on the side wall of the test section using a number of pressure transducers. Figure 22 presents the pressure profile along the nozzle centerline obtained from PSP measurements with the discrete measurement results, shown by square blocks, for various inlet pressures. The transducers correspond to T3, T4, and T5 in Fig. 21. The pressure along the y-axis is non-dimensionlised with the corresponding inlet pressure (P_{inlet}), and the x-axis is non-dimensionlised with the inlet height of the nozzle (h). The rms error was calculated as 3.15%. The rms error was obtained by taking the difference between PSP and “true” static pressure tap values at each of the pressure tap locations and calculating a root mean square (expressed as a percent of the true value) (Taghavi et al., 1999).

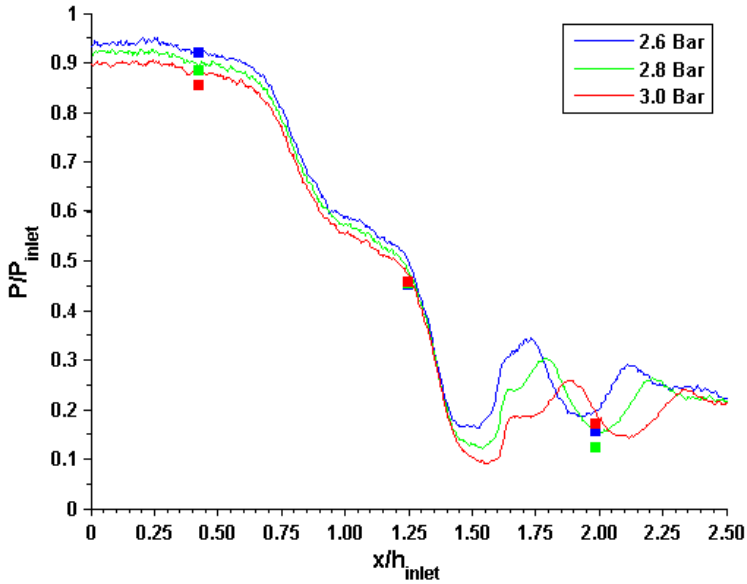

Figure 22: Comparison between discrete measurements and PSP results for various inlet pressures.

Figure 23 represents the PSP results obtained for inlet pressures varying from *1.4-2.4 bar*. As the flow is introduced at low pressures we begin to notice the rise in pressure in the convergent portion the nozzle and the decrease at the exit of the uniform area section due to the acceleration of the flow (Fig. 23(a)). If the pressure difference is further increased the stronger pressure ratio between the inlet and exit accelerates the flow and the variations of subsonic Mach number and static pressure through the duct will be larger.

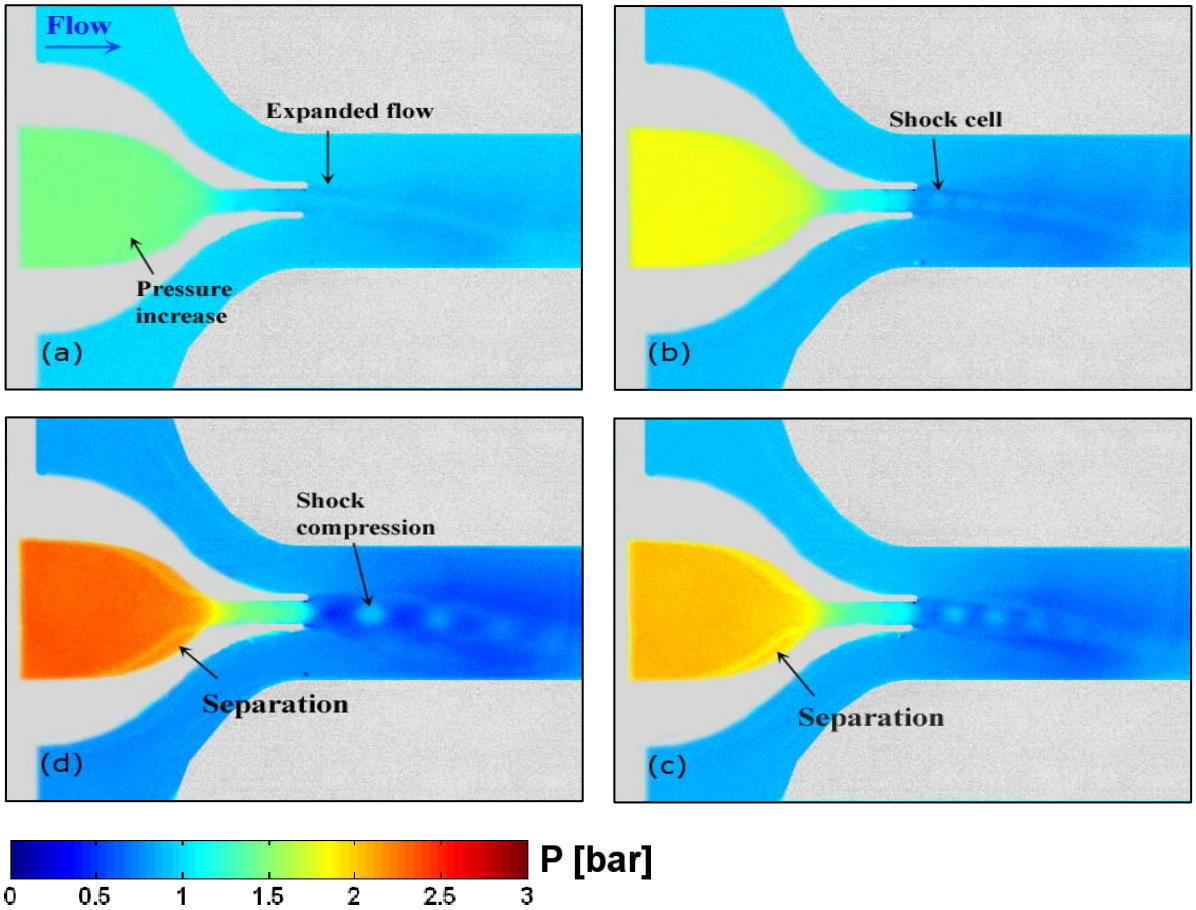

Figure 23: PSP images for P_{inlet} = (a) 1.4 bar, (b) 1.8 bar, (c) 2.0 bar, (d) 2.4 bar.

With further increase of the inlet pressure, the Mach number at the throat cannot increase beyond *M=1*. This is dictated by the area Mach number relation. Hence, the flow properties at the throat and indeed throughout the entire subsonic section of the duct become frozen and the mass flow remains constant. This condition after sonic flow is attained at the throat corresponds to the choked flow condition. As the plenum pressure is increased beyond the choked flow condition, a series of shock cells form in the jet plume, as it can be seen in Fig. 23(b). Figures 23(c) and 23(d), exhibit properties of underexpanded jets since the flow is capable of additional expansion. An underexpanded jet starts with an expansion process where pressure progressively decreases until the shock compression region (Fig. 23(d)) is encountered where pressure jumps to a higher value. Equilibrium of the flow takes place across expansion waves outside the duct, since across the expansion fan the pressure decreases and thus the sudden acceleration of the flow is communicated to the surrounding flow. The supersonic flow is decelerated and the wall static pressure increases through a shock train region.
The separation of the flow along converging portion of the nozzle causes the static pressure to decrease. The regions of flow separation are identified in Figs. 23(c) and 23(d).
Close-ups of the flow corresponding to inlet pressures of *1.8 bar* and *2.4 bar* (similar to Figs. 23(b) and 23(d)) are presented in Fig. 24. The colourbar is adjusted such that the shock structures are easier to discern. Increasing the inlet pressure causes the pressure through the throat to gradually increase; this terminates at the nozzle exit with the formation of expansion fans and consequent shock cells. In Fig. 24(a) we can see three compression zones in full and half of the fourth compression zone, whereas in Fig 24(b) only one compression zone exists. Due to the increase in flow Mach number through the throat, the inclination of the last running expansion fan (relative to the vertical) is greater (Fig. 24(b)).

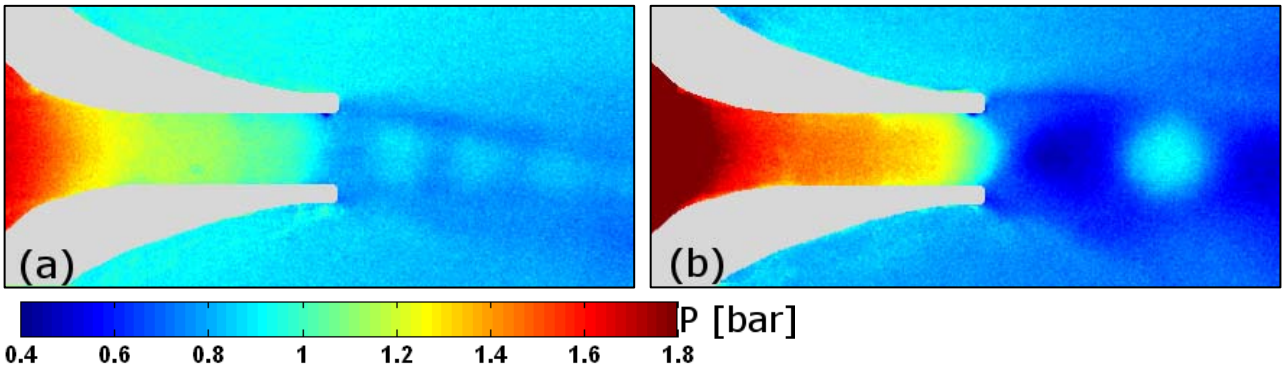

Figure 24: Close-up of throat section for P_{inlet} = (a) 1.8 bar, (b) 2.4 bar.

With increase in plenum pressure, the static pressure along the converging entrance of the nozzle continues to increase. Observing the PSP images of events taking place in Fig. 25, the expansion zones are relatively longer with the pressure within the convergent section continuing to increase. The decrease in wall static pressure is reminiscent of the acceleration of the flow exiting the nozzle. Examining closely Figs. 25(a) and 25(b) we can see how the deflection of the last expansion fan increases relative to the normal with increasing flow Mach number, tending to become parallel to the free stream at higher Mach numbers.

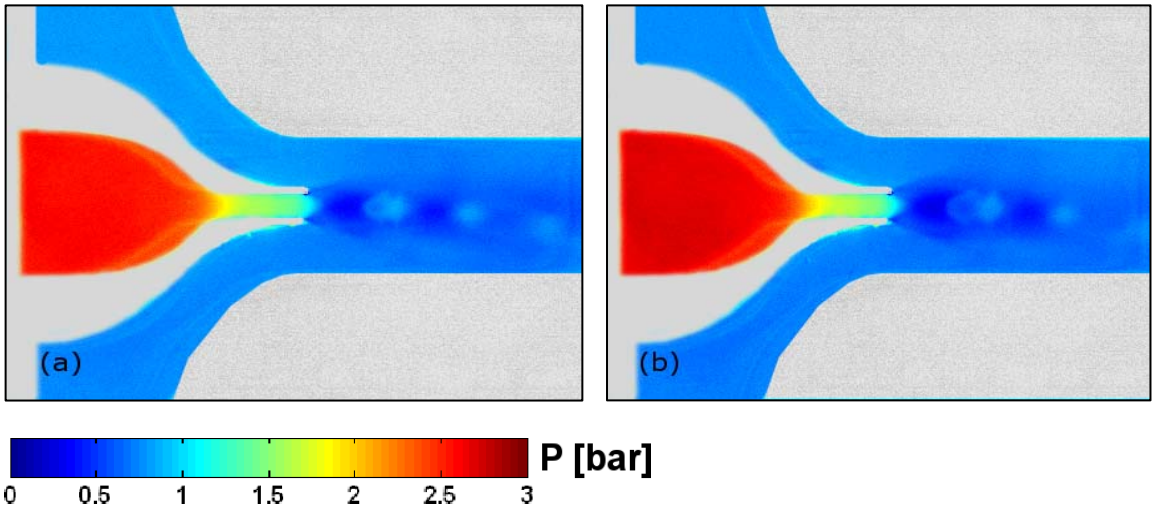

Figure 25: PSP images for P_{inlet} = (a) 2.8 bar, (b) 3.0 bar.

7. PLASMA JET STUDIES

Some preliminary investigations were conducted to assess the effect plasma actuators on jet performance and stability characteristics. All photos were taken at the pick of the plasma discharge cycle. As it can be seen in Fig. 26, the presence of plasma discharges manipulates considerably the stability characteristics of the jet changing its mixing properties and lateral spreading. The jet-only experiments utilised three voltage-frequency settings (10kVpp-5kHz, 50kVpp-5kHz, 50kVpp-33kHz).

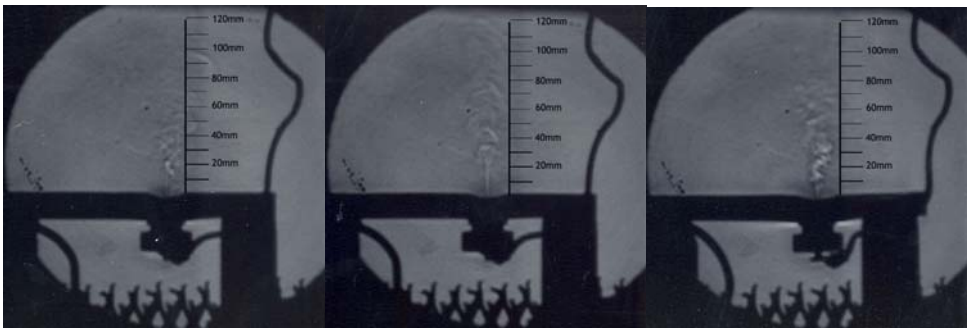

Figure 26: Effect plasma discharge on jet flowfield characteristics.

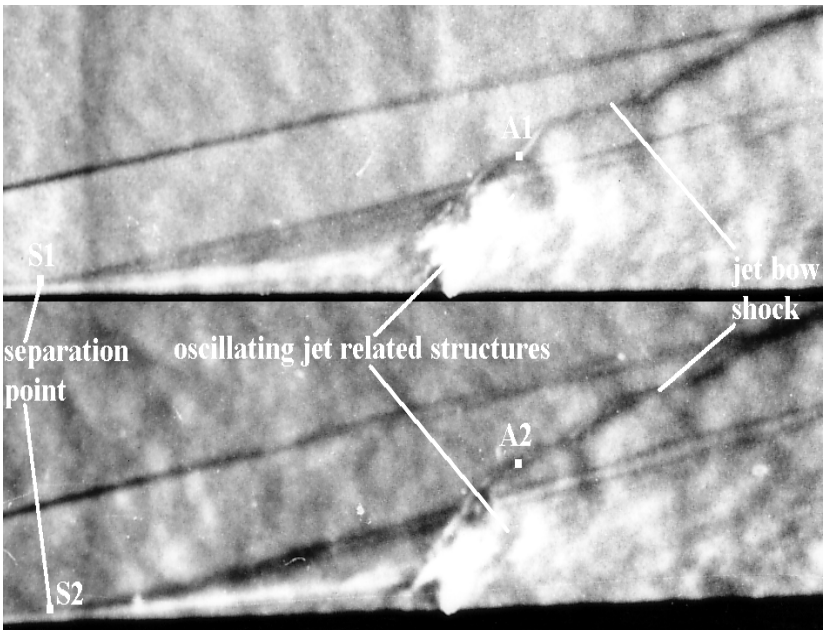

Figure 27: Effect of energy deposition on jet in crossflow interactions.

From Figure 27, the periodic pulsations of the shock front can be seen. These are the product of fluctuations in the separation and jet horseshoe vortices due to plasma actuators operating at 50kVpp-33kHz. The oscillations are convected downstream by the free stream flow and produce the periodic variations in the jet bow shock structure observed in Fig. 27, see for example points A1 and A2. The jet bow shock pulsations cause an oscillatory movement of the jet itself. The jet-related structures are fed into the upstream interaction region and cause a small amplitude of the order of 1mm, oscillatory movement of the separation front, e.g. S1 and S2 in Fig. 27.

8. CONCLUSIONS

1) The global flow features and low frequency motion inside the boundary layer are Reynolds no. dependent (clean case tests).
2) Non-plasma jet oscillations are due to the effects of upstream boundary layer and jet instabilities.
3) Analytical correlations for non-plasma jet lateral spreading, penetration height, and separated flow length were derived, which exhibit good agreement with experimental measurements.
4) The interaction between the jet and the external flow causes a change in surface pressure around the injector.
5) At zero incidence, the shape of the interaction region is a direct function of the shape of the jet bow shock. The jet penetration is less for the sharp plate, whereas the lateral spreading is less for the blunt plate.
6) Leading edge bluntness causes a delay in separation with respect to the equivalent sharp leading edge configuration.
7) The plasma generation system was designed and manufactured.
8) The instrumented jet nozzles were designed and manufactured.
9) The PSP system was validated successfully for high speed jet flow studies.
10) The S/N, seeding quality and uniformity of the PIV system were optimised.
11) The presence of plasma discharges manipulates considerably the stability characteristics of the jet changing its mixing properties and lateral spreading.
12) Energy deposition at the jet orifice creates periodic pulsations of the shock front. The jet-related structures are fed into the upstream interaction region and cause a small amplitude of the order of 1mm, oscillatory movement of the separation front.

Further studies are required to assess in detail the control effectiveness of plasma actuators on the jet-only and jet-in-crossflow cases. It is important to improve S/N, to optimize seeding quality and uniformity, and to determine the effect of seeding on the flow properties inside the settling chamber and test section. Detailed time resolved surface pressure and Pressure Sensitive Paint measurements are necessary to shed further light into the observed phenomena. PIV measurements needs to be conducted for the transverse non-plasma and plasma jets.

Acknowledgment/Disclaimer

This work was sponsored by the Air Force Office of Scientific Research, USAF, under grant/contract number FA8655-07-1-3032. The views and conclusions contained herein are those of the authors and should not be interpreted as necessarily representing the official policies or endorsements, either expressed or implied, of the Air Force Office of Scientific Research or the U.S. Government. Personnel Supported: Mr Erinc Erdem, Graduate Student, University of Manchester, UK, Prof. Konstantinos Kontis, University of Manchester, UK.

REFERENCES

1. Dolling, D. S., *AIAA Journal*, Vol. 36-5, 1998, pp. 725-732.
2. Ganapathisubramani, B., Clemens, N. T., and Dolling, D. S., AIAA paper 2007-1141, 2007.
3. Erengil, M. E. and Dolling, D. S., AIAA paper 1993-3134, 1993.
4. Unalmis, O. H. and Dolling, D. S., *AIAA Journal*, Vol. 36-3, 1998, pp. 371-378.
5. Beresh, S. J., Clemens, N. T., and Dolling, D. S., *AIAA Journal*, Vol. 40(12), 2002, pp. 2412-2422.

6. Kontis, K., Stollery, J.L., *Journal of Spacecraft and Rockets*, Vol. 34, No. 6, pp. 762-768, 1997.
7. Qin, N., Redlich, A., Shock Waves (1999) 9: 87-93.
8. Roberts, G.T., Schuricht, P.H., Mudford, N.R., Shock Waves (1998) 8: 105–112.
9. Powrie, H.E.G., Ball G.J., East R.A., AGARD CP534 (1993) pp. 20-1–20.7.
10. Kumar, D., Stollery, J.L., Smith, A.J., Shock Waves, (1997) 7:1–12.
11. Zukoski, E. E., and Spaid, F. W., *AIAA Journal*, Vol. 2, No. 10, 1964, pp.1689-1696.
12. Mallison, S.G., Reizes, J.A., Hillier, R., *Flow, Turbulence and Combustion* 66: 1–21, 2001.
13. Dickmann, D.A., Lu, F.K., AIAA 2006-3451.
14. Finley P.J., Journal of Fluid Mechanics, Vol.26, p.2, 1966.
15. J. S. Shang, AIAA Journal, Vol. 40, No. 6, June 2002.
16. Shang, J. S., Hayes, J., Wurtzler, K., and Strang,W., *AIAA Journal*, Vol. 36,No. 6, 2001,pp. 1159–1165.
17. Barber, E. A., Jr., *Journal of Spacecraft and Rockets*, Vol. 2, No. 5, 1965, pp. 770–774.
18. Bélanger, J. and Hornung, H.G., *Proceedings of the Nineteenth International Symposium on Shock Waves*, Vol. I. Springer-Verlag, Berlin (1995) pp. 157–162.
19. Payne, M. D., Chrissis, J. W., Pohl, E. A., Bowersox, R. D. W., Gruber, M. R., and Fuller, R. P., AIAA 1999-2251.
20. Gruber, M.R., Nejad, A.S. and Dutton, J.C., AIAA Paper 95-2150.
21. Cassel, L.A., *Journal of Spacecraft and Rockets*, Vol. 40, No. 4, July–August 2003.
22. Bowersox, R., Fan, H., and Lee, D., *Journal of Propulsion and Power*, Vol. 20, No. 2, 2004, pp. 280–287.
23. Tomioka, S., Jacobsen, L., and Schetz, J., *Journal of Propulsion and Power*, Vol. 19, No. 1, January-February 2003, pp. 104–114.
24. Srinivasan, R. and Bowersox, R., AIAA 2004-2698, 2004.
25. Simpkins, P., *Hypersonic Boundary Layers and Flow Fields*, AGARD CP-30, 1968.
26. Kontis, K. and Stollery, J.L., *J Spacecraft and Rockets*, 1997, **34**, pp 762-768.
27. Kumar, D., Stollery, J.L., AIAA-95-6066, 1995.
28. Vermeulen, J.P. and Simeonides, G., VKI TN-181, 1992.
29. Edwards, C.L.W. and Anders, J.B., NASA TN D-4829, 1968.
30. Coet, M.C., Delery, J. and Chanetz, B., *Aerothermochemistry of Spacecraft and Associated Hypersonic Flows*, Proceedings of the IUTAM Symposium/Marseilles (France), International Union of Theoretical and Applied Mechanics, 1992, pp. 234-239.
31. Townsend, J.C., NASA TN D-3290, 1966.
32. Holden, M.S. and Moselle, J.R., AIAA-92-4023, 1992.
33. Kontis, K., *J Thermophysics and Heat Transfer*, 2003, **17**, No. 3, pp. 359-364.
34. Baldwin, B.S. and Lomax, H., AIAA-78-0257, 1978.
35. Kontis, K., Qin, N., Stollery, J.L. and Edwards, J.A., *J Spacecraft and Rockets*, 2000, **37**, No. 1, pp. 21-28.
36. Yee, H.C., NASA TM-101088, Oct. 1989.
37. M. Samimy, J.-H. Kim, I. Adamovich, Y. Utkin, and J. Kastner, AIAA 2006-711.
38. Basu, B.J., Optical oxygen sensing based on luminescence quenching of platinum porphyrin dyes doped in ormosil coatings, Sensors and Actuators B, 123 (2007), 568-577.
39. Bell, J. H., Schairer, E. T., Hand, L. A. and Mehta, R. D., Surface pressure measurements using luminescent coatings, Annual Review of Fluid Mechanics, 33 (2001), 155-206.
40. Carroll, B. F., Abbitt, J. D., Lucas, E. W. and Morris, M. J., Step response of pressure-sensitive paints, AIAA Journal, 34 (1996), 521-526.
41. Etele, J., Parent, B. and Sislian, J. P., Analysis of increased compression through area constriction on ejector-rocket performance, J. Spacecraft and Rockets, 44 (2007), 355-364.
42. Eustace, V. A., A study of two-dimensional supersonic air ejector systems, PhD Thesis, The University of Manchester Institute of Science and Technology, 1969.
43. Huang, C.Y., Gregory, J.W., and Sullivan, J.P., Flow visualization and pressure measurement in micronozzles, J. Visualization, 10 (2007), 123-130.
44. Kweon, Y-H., Miyazato, Y., Aoki, T. and Kim, H-D., Experimental investigation of nozzle exit reflector effect on supersonic jet, Shock Waves, 15 (2006), 229-239.

45. Lepicovsky, J. and Bencic, T. J., Use of pressure-sensitive paint for diagnostics in turbo-machinery flows with shocks, Experiments in Fluids, 33 (2002), 531-538.
46. Liu, T. and Sullivan, J. P., Pressure and temperature sensitive paints (2005), Springer, Berlin.
47. Liu, T. and Sullivan, J. P., In situ calibration uncertainty of pressure-sensitive paint, AIAA Journal, 41 (2003), 2300-2302.
48. Love, E. S., Grigsby, C. E, Lee, L. P. and Woodling, M. J., Experimental and theoretical studies of axisymmetric free jets, NASA technical report, (1959), NASA TR R-6.
49. McLachlan, B.G., Bell, J.H., Park, H., Kennelly, R.A., Schreiner, J.A., Smith, S.C., Strong, J.M., Gallery, J. and Gouterman, M., Pressure-sensitive paint measurements on a supersonic high-sweep oblique wing model, Journal of Aircraft, 32 (1995), 217-227.
50. Moshasrov, V., Radchenko, V. and Fonov, S., Luminescent pressure sensors in aerodynamic experiments, (1998), Central Aerodynamic Institute (TsAGI).
51. O'keeffe, G., MacCraith, B. D., McEvoy. A. K., McDonaghk C. M. and McGilp, J.F., evelopment of a LED-based phase fluorimetric oxygen sensor using evanescent wave excitation of a sol-gel immobilized dye, Sensors and Actuators B 29 (1995), 226-230.
52. Panda, J. and Seasholtz, R. G., Measurement of shock structure and shock-vortex interaction in underexpanded jets using Rayleigh scattering, Physics of Fluids, 11 (1999), 3761-3777.
53. Raju, C. and Viswanath, P. R., Pressure-sensitive paint measurements in a blowdown wind tunnel, Journal of Aircraft, 42 (2005), 908-915.
54. Taghavi, R. R., Raman, G. and Bencic, T. J., Mixer-ejector wall pressure and temperature measurements based on photoluminescence, AIAA Journal, 40 (2002), 745-750.
55. Taghavi, R., Raman, G. and Bencic, T., Pressure sensitive paint demonstrates relationship between ejector wall pressure and aerodynamic performance, Exp. in Fluids, 26 (1999), 481-487.
56. Tang, Y., Tehan, E.C., Tao, Z. and Bright, F. V., Sol-gel-derived sensor materials that yield linear calibration plots, high sensitivity, and long-term stability, Analytical Chemistry 75 (2003), 2407-2413.
57. White, F. M., Fluid Mechanics, (2003), McGraw-Hill.